

RAPID, STRONGLY MAGNETIZED ACCRETION IN THE ZERO-NET-VERTICAL-FLUX SHEARING BOX

JONATHAN SQUIRE 

Physics Department, University of Otago, Dunedin 9010, New Zealand

ELIOT QUATAERT

Department of Astrophysical Sciences, Princeton University, Princeton, NJ 08544, USA

PHILIP F. HOPKINS

TAPIR, Mailcode 350-17, California Institute of Technology, Pasadena, CA 91125, USA

Version March 10, 2025

Abstract

We show that there exist two qualitatively distinct turbulent states of the zero-net-vertical-flux shearing box. The first, which has been studied in detail previously, is characterized by a weakly magnetized ($\beta \sim 50$) midplane with slow periodic reversals of the mean azimuthal field (dynamo cycles). The second, the ‘low- β state,’ which is the main subject of this paper, is characterized by a strongly magnetized $\beta \sim 1$ midplane dominated by a coherent azimuthal field with much stronger turbulence and much larger accretion stress ($\alpha \sim 1$). The low- β state emerges in simulations initialized with sufficiently strong azimuthal magnetic fields. The mean azimuthal field in the low- β state is quasi steady (no cycles) and is sustained by a dynamo mechanism that compensates for the continued loss of magnetic flux through the vertical boundaries; we attribute the dynamo to the combination of differential rotation and the Parker instability, although many of its details remain unclear. Vertical force balance in the low- β state is dominated by the mean magnetic pressure except at the midplane, where thermal pressure support is always important (this holds true even when simulations are initialized at $\beta \ll 1$, provided the thermal scale height of the disk is well resolved). The efficient angular momentum transport in the low- β state may resolve long-standing tension between predictions of magnetorotational turbulence (at high β) and observations; likewise, the bifurcation in accretion states we identify may be important for understanding the state transitions observed in dwarf novae, X-ray binaries, and changing-look AGN. We discuss directions for future work, including the implications of our results for global accretion disk models and simulations.

Subject headings: accretion, accretion disks — MHD — turbulence — instabilities — quasars: general — X-rays: binaries

1. INTRODUCTION

Accretion disks power a variety of the most luminous and interesting sources in the Universe, forming the crucial intermediary that allows matter to lose its angular momentum and fall into a central object. Hotter systems, such as quasars, X-ray binaries, and dwarf novae are mostly well ionized, with the required outwards angular momentum transport thought to be dominated by turbulence induced by the magnetorotational instability (MRI; Balbus & Hawley 1991). Significant work has thus focused on understanding the nonlinear turbulent saturation of the MRI, particularly the so-called Shakura & Sunyaev (1973) α parameter, which quantifies the rate of angular momentum transport. Local and global simulation studies have found α values between $\simeq 0.001$ and $\simeq 1$ depending on the physical parameters and resolution (Hawley et al. 1995; Stone et al. 1996; Fromang 2010; Bai & Stone 2013; Ryan et al. 2017), as well as various more complex pictures involving e.g., transport via winds and coherent fields (e.g., Lesur et al. 2013; Zhu & Stone

2018). Difficulties in the agreement between theory and observations remain (e.g., King et al. 2007; Tetarenko et al. 2018) and it is fair to say that our understanding of accretion remains incomplete.

An intriguing possibility for addressing related observational and theoretical challenges is that disks may host magnetic fields with pressures comparable to, or even exceeding, the gas pressure. By supporting the gas against vertical collapse, such superthermal fields enhance the disk’s thermal, viscous, and gravitational stability compared to standard models, potentially allowing much higher accretion rates (e.g., Pariev et al. 2003; Begelman & Pringle 2007; Oda et al. 2009; Sądowski 2016). A net vertical flux (NVF) threading the disk appears to aid in the growth and sustenance of such fields via the MRI (e.g., Miller & Stone 2000; Suzuki & Inutsuka 2009; Zhu & Stone 2018; Mishra et al. 2022), but presumably requires the coherent vertical field to pre-exist as a property of the central object. However, even without a clear source of NVF, various global simulation studies have reported the formation of (apparently) stable, rapidly accreting disks with strong toroidal mag-

netic fields (Machida et al. 2006; Gaburov et al. 2012; Sądowski 2016; Guo et al. 2024), suggesting that such states may be a common outcome of accretion. A striking recent example is the “hyper-refined” simulation of Hopkins et al. (2024a) and Hopkins et al. (2024b) (hereafter H+24), which traced gas inflow from cosmological initial conditions on galactic scales into a sub-pc steady state accretion disk. The disk’s toroidal magnetic field becomes highly superthermal, with a plasma β (the ratio of thermal to magnetic pressure) of $\sim 10^{-4}$. This allows it to avoid fragmentation across a wide range of radii ($\gtrsim 1$ pc) while sustaining very high accretion rates $\alpha \gg 1$. The magnetized system’s enhanced stability arises because magnetic support and strong turbulence produce a thicker disk, enabling higher inflow rates for similar surface densities, or equivalently, lower densities for a given mass supply rate¹ (Hopkins et al. 2024c).

The global results discussed above fundamentally rely on the disk being *able* to sustain $\beta \lesssim 1$ (or $\beta \ll 1$) magnetic fields against destruction by turbulence or vertical escape from the disk. Some previous works have argued that a $\beta \lesssim 1$ midplane cannot be maintained without NVF, because strong toroidal fields rise rapidly (in several orbits) out of the disk midplane (Salvesen et al. 2016a; Fragile & Sądowski 2017). While H+24 and Gaburov et al. (2012) argue that the toroidal field in their simulations is replenished primarily via simple advection from further out in the disk, if loss processes acted more rapidly than the accretion of more flux, the system would lose its field, undermining all other aspects of the strongly magnetized solution. As mentioned above, while simulations with NVF do maintain a $\beta \lesssim 1$ midplane in both local (Suzuki & Inutsuka 2009; Bai & Stone 2013) and global (Zhu & Stone 2018; Mishra et al. 2020) setups, the global solutions seem to possess a morphology that is rather different from H+24 and other $\beta \lesssim 1$ global simulations without external NVF. In addition, as far as we are aware, NVF simulations have never been observed to sustain $\beta \ll 1$ magnetic fields, as seen in H+24 and Guo et al. (2024).

These considerations motivate a re-examination of whether strong magnetic fields can be sustained against vertical escape without NVF in the simplest viable model: the local stratified shearing box. Early results from Johansen & Levin (2008) suggested that zero-net-vertical-flux (ZNVF) boxes *could* sustain a toroidal field with $\beta \sim 1$ against escape. However, this was challenged by Salvesen et al. (2016a), who showed that Johansen & Levin (2008)’s results were affected by their vertical boundary conditions. When open boundaries were used, Salvesen et al. (2016a) argued that $\beta \sim 1$ purely toroidal fields always escape, leaving behind a midplane with $\beta \sim 50$. Here, using a setup similar to Salvesen et al. (2016a)’s but with stronger initial toroidal fields, we argue that a ZNVF $\beta \sim 1$ state *can*, in fact, self-sustain in the local shearing box and — as a consequence — that vertical flux is not a requirement for large accretion stresses. The simulations resemble those of Johansen & Levin (2008) but (crucially) differ in that flux continu-

ously escapes from the system’s top and bottom boundaries while being regenerated at the midplane. Our solutions are also similar to those of H+24, Gaburov et al. (2012), and Guo et al. (2024) in various relevant respects, although they do not sustain a $\beta \ll 1$ midplane in steady state unless numerically limited (we provide some evidence and commentary on additional global effects that could act to decrease β to be $\ll 1$). Compared to global simulations, our results thus provide a much simpler way to study the main physical mechanisms that could enable strongly magnetized accretion.

An interesting outcome of our findings is the existence of a sudden and sharp transition between two radically different forms of shearing-box turbulence. The first — termed the “high- β state” here, and explored in many previous works (e.g., Miller & Stone 2000; Guan et al. 2009; Simon et al. 2012) — involves a thermal-pressure dominated ($\beta \simeq 50$) midplane, with super-Alfvénic turbulence, cyclic reversals of the weak mean toroidal field over $\simeq 10$ -orbit timescales (often termed ‘MRI dynamo cycles’), and weak transport (angular-momentum stress $\alpha \simeq 0.02$). The second — termed the “low- β state” and the subject of this work — involves a continuous (non-cyclic) strong toroidal field with $\beta \lesssim 1$, modestly sub-Alfvénic turbulence, and much stronger angular momentum transport ($\alpha \simeq 0.5$). So long as the box has sufficient vertical extent (which is required to realize the low- β state), the transition between the two is determined by the initial total flux available to the system: if the system starts out sufficiently strongly magnetized, it can sustain this low- β state; if the magnetic field is too weak, all of the flux inevitably escapes, transitioning into the high- β state. This bifurcation may have interesting implications for understanding state transitions observed in X-ray transients and dwarf novae (e.g., Smak 1984; Hameury 2020), suggesting that additional magnetic flux in almost any configuration (not just a coherent vertical field in particular) could trigger high accretion rates. The same abrupt changes in angular momentum transport efficiency could be important for understanding the emerging class of changing-look active galactic nuclei (Ricci & Trakhtenbrot 2023).

Our work here is organized around a wide set of stratified shearing-box simulations starting from initial conditions with strong ($\beta \lesssim 1$) toroidal fields. In order to convincingly characterize the low- β state and transition, a range of different simulations are needed, which also leads to a proliferation of complications about the effects of numerical options, initial conditions etc. To provide the reader with a “road map” before starting, in §2 we outline, without providing any detailed interpretation, various outcomes of our numerical experiments that inform our results and interpretation. We then describe the numerical setup in §3, with the various different numerical options, boundary conditions, and initial conditions described in §3.2 and §3.3. These are mostly chosen to be standard, matching previous works. For reference in the simulation analysis, we also provide an overview of strongly magnetized vertical equilibria (§3.1), as well as a recapitulation of the MRI and Parker instabilities (§4), which we argue are key to the field-sustenance mechanism, consistent with past studies (Johansen & Levin 2008; Kudoh et al. 2020; Held et al. 2024). Our main results on the properties of the low- β state are detailed in

¹ Indeed, the simple numerical experiment of removing the magnetic field in H+24 yields a vastly different solution, which fragments on small scales as expected and may not even accrete (see H+24 figures 28-30).

§5, while those related to the field-sustenance mechanism (dynamo) are presented in §6. Finally, we summarize and conclude in §7 with a detailed discussion of how our results apply to previous global results and $\beta \ll 1$ fields in §7.3. The appendices explore the effect of numerical options (box aspect ratio, resolution, and an artificial density floor) and present various subsidiary results.

2. SUMMARY OF KEY BEHAVIORS

In §5 and §6, we explore results from a range of different setups in order to build a picture of the local behavior of the strongly accreting, low- β state. However, various factors add complexity to the story (e.g., initial conditions, boundary conditions, resolution); so, for reference, we provide a list of the key behaviors that will be discussed. The following describes various observations from the set of numerical experiments; a more detailed interpretation of the important physics will be given in the results (§5-§6) and discussion (§7).

1. There exist (at least) two qualitatively different turbulent states of ZNVF shearing-box turbulence. The first, which has been regularly studied previously, is characterized by a weakly magnetized ($\beta \sim 50$) midplane with slow periodic reversals of the mean azimuthal field (dynamo cycles). The second, which is the main subject of this article, is characterized by a strongly magnetized $\beta \sim 1$ midplane dominated by a coherent azimuthal field in quasi steady state (no cycles), with much stronger turbulence and much larger accretion stress α .
2. In the absence of a vertical field, the transition between these two states is primarily controlled by the magnetization of the system: if the system has sufficient magnetic flux available such that it retains $\beta \lesssim 1$ in the midplane once it reorganizes from its initial state, it can maintain this steady state; if β in the midplane rises above $\simeq 1$, it inevitably loses nearly all of its flux and transitions into the high- β weakly accreting state.
3. Turbulence in the low- β state is trans-Alfvénic with $\delta u/v_A \simeq 0.3$ across its full vertical profile, becoming highly supersonic in lower- β regions above/below the midplane. Its profile is well fit by a simple model based on the MRI and Parker instability.
4. By virtue of point 3, the vertical equilibrium of the low- β state is dominated by the mean magnetic pressure, except within $\lesssim H_{\text{th}}$ of the midplane, where the density collapses down to approximately its (Gaussian) thermal profile. Above the midplane, both azimuthal field and density are approximately power laws.
5. The low- β magnetized state remains robust regardless of the chosen vertical boundary conditions, as long as material and magnetic flux can escape the domain. It is also insensitive to the vertical domain size, provided the domain is sufficiently large compared to H_{th} . However, when starting from initial conditions that lie near those at which the system changes between the low- and high- β state (with constant- β Gaussian initial conditions, this occurs when $\beta \approx 0.1$ initially), the transition can depend on resolution and boundary conditions, presumably because they affect the efficiency of the flux transport through the vertical domain boundaries.
6. A sufficiently large domain in the azimuthal direction is necessary to sustain the low- β state. The radial domain size does not appear to have a significant influence.
7. With progressively more vertical magnetic flux, the ZNVF low- β state changes into the stratified low- β NVF state described in previous works (Suzuki & Inutsuka 2009; Bai & Stone 2013; Salvesen et al. 2016b). This transition happens for $\beta_z \lesssim 1000$, viz., a vertical field with $\beta_z \geq 1000$ makes little difference to α or the morphology of the low- β state. Consistent with past works, stronger vertical fields cause a more strongly magnetized midplane ($\beta < 1$), with a larger α that is dominated by the contribution from the mean magnetic fields.
8. The net azimuthal field in the low- β state is actively sustained by a dynamo mechanism. Strong turbulent diffusion and vertical outflows continuously remove the flux out of the top and bottom boundaries of the simulation. This azimuthal flux loss is balanced by shearing of the radial field, which is replenished from the azimuthal field by turbulence to maintain steady state.
9. Both rotation and the mean shear flow are needed to maintain the low- β strongly accreting state.
10. Systems that are initially even more strongly magnetized, with $\beta \ll 1$, remain in quasi-equilibrium while relaxing back down towards $\beta \simeq 1$ in the midplane. As this occurs, the density profile collapses towards the thermal scale height. This relaxation process is relatively slow, operating on a timescale of 5-10 orbits.
11. If the numerical resolution is sufficiently coarse that the density scale height near the midplane becomes limited by grid resolution before thermal pressure, the system reaches a $\beta \ll 1$ steady state with supersonic (though still sub-Alfvénic) turbulence in the midplane. The mean fields are sustained via a similar dynamo mechanism to that which operates when the scale-height near the midplane is well resolved. This suggests that if the collapse of the density to a thermally supported region is halted by some mechanism (e.g., another source of turbulence), the system may self-sustain a $\beta \ll 1$ state.
12. The mechanism that closes the low- β ZNVF dynamo loop, generating a mean radial field from the mean azimuthal field, remains unclear. Although the turbulence has a net helicity away from the midplane, suggesting that a dynamo “alpha effect” could operate, the sign of the net helicity is β dependent and not always that needed to sustain the mean field (see also Tharakkal et al. 2023).

In addition to these observations relating to the low- β ZNVF state, our numerical experiments have revealed some subsidiary points relevant to accretion physics in other contexts:

14. In the high- β state, dynamo cycles (temporal reversals in the sign of the mean azimuthal field) persist in the absence of rotation so long as mean shear is present, with or without NVF. This shows that, despite being traditionally associated with the MRI, differential rotation and the MRI are sufficient but not necessary for producing dynamo cycles.
15. With NVF, the strong mean azimuthal fields are effectively sustained as a single MRI channel mode that stretches across the full vertical extent of the domain. While the symmetry of this state is likely inconsistent with global constraints (Bai & Stone 2013), global simulations (Zhu & Stone 2018; Mishra et al. 2020) appear to exhibit a similar global channel mode but with opposite parity, with the ordered radial magnetic field maintained by an equatorial outflow and inflows away from the midplane.

3. THEORY & METHODS

Our numerical methods and setup are designed to be as standard as possible in order to understand the relationship of our results to previous works. We use the ATHENA++ code (Stone et al. 2020) with the shearing box method, thus modelling a local patch of the disk in Cartesian coordinates (Hawley et al. 1995). We define the Cartesian coordinates in the standard way: $x \equiv (R - R_0)/L_0$, $y \equiv R_0\phi/L_0$, $z \equiv z/L_0$, where R , ϕ , and z refer to the usual cylindrical coordinate system for a disk in the $z = 0$ plane. The parameter L_0 allows the local coordinate system to be rescaled to a convenient length scale, which we will generally take to be that of a magnetized equilibrium for reasons discussed below.

We solve the isothermal shearing-box MHD equations:

$$\frac{\partial \rho}{\partial t} = -\nabla \cdot (\rho \mathbf{U}), \quad (1a)$$

$$\frac{\partial(\rho \mathbf{U})}{\partial t} = -\nabla \cdot \left[\rho \mathbf{U} \mathbf{U} - \frac{\mathbf{B} \mathbf{B}}{4\pi} + \left(c_s^2 \rho + \frac{B^2}{8\pi} \right) \mathbf{1} \right] + 2q\rho\Omega^2 x \hat{x} - 2\Omega \hat{z} \times (\rho \mathbf{U}) - \rho \Omega^2 z \hat{z}, \quad (1b)$$

$$\frac{\partial \mathbf{B}}{\partial t} = \nabla \times (\mathbf{U} \times \mathbf{B}). \quad (1c)$$

Here \mathbf{B} is the magnetic field, $\mathbf{U} = -q\Omega x \hat{y} + \mathbf{u}$ is the total flow velocity (including the background shear $-q\Omega x \hat{y}$), ρ is the mass density, Ω is the local rotation rate, which is the natural time unit for the system, $q \equiv -d \ln \Omega / d \ln R = 3/2$ for a Keplerian disk, and c_s is the (constant) sound speed.

Although idealized, many studies have shown that the turbulent dynamics induced by Eqs. (1a) to (1c) are widely varied and dynamically complex, involving the natural generation of long-time coherent large-scale fields and flows, and other complex features. The system also has various undesirable properties such as solutions that depend on the vertical boundary conditions, resolution, and box size (e.g., Simon et al. 2012; Shi et al. 2016;

Ryan et al. 2017), as well as the obvious neglect of potentially important global effects (e.g., field-line curvature). For our purposes, it retains two important advantages compared to global simulations: first, it is cheaper computationally than global simulations for similar disk resolutions; second, it provides a much simpler and more controllable testbed for understanding the key physics at play in the system, particularly in steady state. We will see that vertical stratification is absolutely crucial to the physics we describe, meaning that the yet simpler unstratified version of the shearing box would be unsuitable.

3.1. Static vertical equilibria in the local shearing box

The form of the magneto-static solutions to Eq. (1b) will play an important role in our narrative and numerical setup, so are helpful to outline in detail here. Assuming $\mathbf{u} = 0$ and that all variables are time independent and depend only on z , Eq. (1a) is trivial, Eq. (1c) just implies $B_x = 0$, while Eq. (1b) becomes

$$\beta \frac{d \ln P_{\text{th}}}{dz} + \frac{d \ln P_B}{dz} + \beta \frac{2z}{H_{\text{th}}^2} = 0. \quad (2)$$

Here $P_{\text{th}} \equiv c_s^2 \rho$ is the thermal pressure, $P_B \equiv B^2/8\pi$ is the magnetic pressure, $\beta(z) \equiv P_{\text{th}}/P_B$, and $H_{\text{th}}^2 \equiv 2c_s^2/\Omega^2$ is the thermal scale height. We will find that the azimuthal field dominates strongly over the other components. This implies that so long as the turbulence is modestly subsonic where $\beta \gtrsim 1$ and modestly sub-Alfvénic where $\beta \lesssim 1$, then Eq. (2) establishes the relationship between ρ and $B_y \approx \sqrt{8\pi P_B}$. We will also see that the mean vertical outflows that develop do not provide significant contributions to the overall pressure balance, further justifying the magneto-static assumption.

The simplest class of solutions to Eq. (2) comes from assuming β remains constant with height. Then $P_B = P_{\text{th}}/\beta$ and Eq. (2) becomes $(1 + \beta^{-1})d \ln P_{\text{th}}/dz = -2z/H_{\text{th}}^2$ with solution

$$\rho \propto P_{\text{th}} \propto B_y^2 \propto \exp(-z^2/H_{\beta}^2), \quad (3)$$

where $H_{\beta}^2 \equiv H_{\text{th}}^2(1 + \beta^{-1})$. As expected, this reduces to the thermal profile, $\rho \propto \exp(-z^2/H_{\text{th}}^2)$, as $P_B \rightarrow 0$ ($\beta \rightarrow \infty$), but the profile widens with decreasing β as the magnetic field provides more pressure support.

However, although we use Eq. (2) for most initial conditions, it does not even slightly resemble the profiles that arise dynamically in our simulations, which become increasingly magnetically dominated away from the midplane. Given that if $\beta \ll 1$, the system has no way to know about the sound speed and is thus ignorant of H_{th} , which is the only length scale in Eq. (2), the $\beta \ll 1$ limit must be described by scale-free power-law solutions. Inserting the ansatz $P_B \propto z^{-a}$ and $P_{\text{th}} \propto z^{-b}$, we see that the first term in Eq. (2) must become subdominant to the others at large z , leading to $\beta \propto z^{-2}$ and

$$P_B \propto z^{-a}, \quad P_{\text{th}} \propto z^{-a-2}, \quad \text{for} \quad \frac{z^2}{H_{\text{th}}^2} \gg \frac{a}{2} + 1 \quad (4)$$

(i.e., $b = a+2$). Note that this also implies $v_A^2 = 2\Omega^2 z^2/a$ in order to satisfy Eq. (2). In such an equilibrium, the magnetic field provides all of the pressure support while

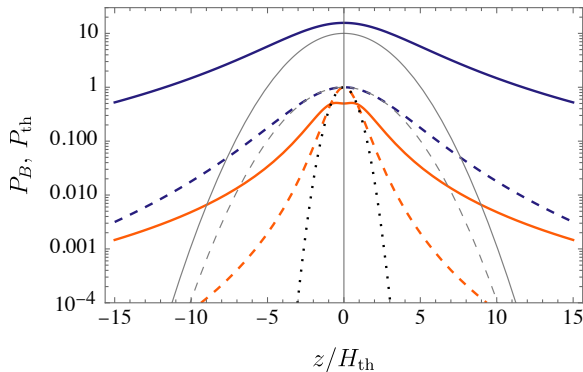


FIG. 1.— Various magneto-static equilibrium solutions to Eq. (2), showing P_B (solid lines) and P_{th} (dashed lines). Colored line pairs show the Lorentzian-like equilibrium (5) with $a = 3$; the blue curves show $H/H_{th} = 5$, such that $\beta(z=0) \approx 0.1$, and the orange curves show $H/H_{th} = 1.5$, which is just below where P_B develops a midplane dip and $\beta(z=0) > 1$ (see text). The dotted black line shows the thermal density profile $\exp(-z^2/H_{th}^2)$ and the thin gray curves show the constant- β equilibrium (3) with $\beta = 0.1$ ($H_\beta \approx 3.3H_{th}$), as used to initialize most simulations. All profiles are normalized with $P_{th}(z=0) = 1$ for ease of comparison.

the gas just provides the mass for the gravitational field. The idea can be generalized to the full range of z by regularizing the P_{th} profile at $z = 0$ as in a Lorentzian function. We thus replace z^2 with $z^2 + H^2$, where H is the density profile’s width near $z = 0$, solving Eq. (2) to yield,

$$P_{th} = \mathcal{N}_a \frac{\rho_0 c_s^2}{\sqrt{\pi}} \frac{H^{a+2}}{(z^2 + H^2)^{(a+2)/2}},$$

$$P_B = \mathcal{N}_a \frac{\rho_0 \Omega^2}{\sqrt{\pi} a} \frac{H^{a+2}(z^2 + H^2 - aH_{th}^2/2)}{(z^2 + H^2)^{(a+2)/2}}. \quad (5)$$

This solution is valid for all z , asymptoting to Eq. (4) at large z , and the normalization factor $\mathcal{N}_a = \Gamma(a/2 + 1)/\Gamma(a/2 + 1/2)$ ensures $\int dz \rho = \rho_0 H$. Equation (5) is useful for understanding the profiles observed in simulations, as well as providing a different equilibrium initial condition to test the robustness of our findings. From the expression for P_B it is clear that the profile is physical only for $H > \sqrt{a/2}H_{th}$, since otherwise P_B becomes negative as z approaches 0. This is a consequence of the fact that if ρ becomes *steeper* than the thermal profile, P_B must provide an inwards force instead of outwards support, causing a dip in P_B near the midplane when $H^2 \leq (a+2)H_{th}^2/2$ (otherwise P_B increases monotonically to $z = 0$). Also useful are expressions for the density scale height (defined such that $H_\rho = H_{th}$ for a thermal profile), $H_\rho \equiv \sqrt{\pi}(\rho_0 H)^{-1} \int dz |z| \rho = 2\mathcal{N}_a H/a \approx H$, and the midplane β , $\beta(z=0) = a/(2H^2/H_{th}^2 - a)$. These show that at large H/H_{th} the solution has a wide density profile, $H_\rho \gg H_{th}$, and satisfies $\beta \ll 1$ everywhere, including in the midplane. These properties are highlighted in Fig. 1, which compares the solutions (5) to Gaussian equilibria.

3.2. Boundary conditions

In all simulations we use periodic boundary conditions in y , and “shear-periodic” boundary conditions in x , whereby quantities are periodic in the frame that remains stationary on the background shear flow $-q\Omega x \hat{y}$.

However, previous works have shown significant dependence of results on the vertical boundary conditions (e.g., Johansen & Levin 2008; Gressel 2013; Salvesen et al. 2016a; Coleman et al. 2017), so we use a number of different choices through this work. All boundary conditions set u_x , u_y , and B_z to have zero gradient at the vertical boundary, and set the vertical flow u_z to have zero gradient unless there is an inflow ($u_z z < 0$), in which case it is set to $u_z = 0$ (Stone et al. 1996). The conditions on ρ , B_x , and B_y are as follows, with the naming scheme used to label simulations in table 1:

Outflow: Zero-gradient boundary conditions for B_x and B_y , while ρ is extrapolated into the ghost cells assuming the initial hydrostatic equilibrium as $\rho(z) = \rho_e \exp(-z^2/H_\beta^2)/\exp(-z_e^2/H_\beta^2)$ (where the z_e and ρ_e here refer to the values at the boundary). Following Simon et al. (2011), these boundary conditions have been widely used and allow the total toroidal and radial magnetic flux within the system to vary.

Simon13: Following Simon et al. (2013) and Salvesen et al. (2016a), these are the same as Outflow, except that they also extrapolate B_x and B_y similarly to the density, with $B_i(z) = B_{i,e} \exp(-z^2/H_\beta^2)/\exp(-z_e^2/H_\beta^2)$. This enhances the removal of magnetic flux from the domain.

Lesur13: Following Lesur et al. (2013), these set $B_x = 0$ at the boundaries and use zero-gradient conditions for ρ and B_y . These boundary conditions are designed to enable winds to form more efficiently, better approximating global simulations.

Power-law: Motivated by the low- β equilibria discussed above (Eq. (4)), B_x and B_y are extrapolated into the ghost cells as $B_i(z) = B_{i,e} |z/z_e|^{-a/2}$ and ρ is extrapolated as $\rho(z) = \rho_e |z/z_e|^{-a-2}$. We set $a = 3$, which is approximately the index observed at large $|z|$ in our simulations.

Outflow, Simon13, and Power-law effectively differ only in the gradient of \mathbf{B}_\perp and ρ assigned at the boundary, as set by the various extrapolation techniques. For context, the Simon13 hydrostatic scheme (Gaussian extrapolation) is most extreme, fixing quantities to larger negative gradients; the power-law scheme is more moderate, while outflow conditions (with zero gradient) are the least extreme. From a close examination of the shape of ρ near the boundaries with Outflow or Simon13, it is clear that the latter forces the profile to be steeper than is natural. This was the primary motivation for the new Power-law scheme — to disturb the solution as little as possible from the profiles that are naturally set up in coronal regions above the midplane.

Overall, we will see that our results are mostly independent of these vertical boundary condition choices, aside from minor changes to time-averaged vertical profiles and α . The solution can be strongly impacted by other choices — for instance, conditions that do not allow the escape of magnetic flux, or those that allow inflows ($u_z z < 0$ at the boundaries) — but these mostly cause features that would be expected to be unphysical in a global setting.

3.3. Initial conditions and numerical setup

Following [Salvesen et al. \(2016a,b\)](#), most of our simulations are initialized with the magnetized constant- β equilibrium (3). Most simulations use a vertical domain size $z \in (-L_z/2, L_z/2)$ with $H_\beta^2 = 2$ and $L_z = 10$, giving significant space away from the midplane to form a low- β corona (it transpires that this is necessary to maintain the low- β state). Based on the results of [Simon et al. \(2013\)](#) and subsequent works, we use $L_x = L_z$ and $L_y = 2L_z$ for most runs, but also test the effect of increasing and decreasing both L_x and L_y by a factor of two (App. A). The equilibrium is then defined by its initial $\beta = \beta_{y0} = 8\pi P_{\text{th}}/B_y^2$, which sets the simulation's isothermal sound speed as $c_s^2 = \Omega^2 H_\beta^2 (1 + \beta^{-1})^{-1}$. In table 1, we label simulations by this initial β , although the midplane β invariably increases significantly from this initial value as the field redistributes and flux is lost through the boundaries.

In some simulations, we additionally add a weak initial radial field of strength $B_x^2 = 8\pi P_{\text{th}}/\beta_{x0}$. This radial field takes the same spatial form as B_y (i.e., $B_x/B_y = \sqrt{\beta/\beta_x}$), and is sufficiently weak that it hardly modifies the equilibrium; however, it is sheared at early times, strengthening B_y , thus effectively adding extra azimuthal flux. Since, like B_y , B_x can escape the boundary, the details of the initial form of B_x do not persist into the saturated state, other than its role in determining whether the weakly or strongly magnetized solution is reached. Two other simulations, labelled ‘Lor’ in table 1, are initialized from the power-law equilibrium Eq. (5) using different H/H_{th} , and thus different midplane β . Finally, some simulations also include a vertical flux via a constant B_z , which is conserved through the simulation. These are parameterized by $\beta_z \equiv 8\pi c_s^2 \rho(z=0)/B_z^2$ in the standard way.

Nearly all simulations use the piecewise parabolic method with the Van-Leer time integrator and the basic HLL Reimman solver. Although this solver is more diffusive than the HLLD solver, we have found this low- β turbulence to be rather sensitive to numerical instabilities, also requiring very conservative choices for the CFL timestep criterion. The strongly magnetized simulations are also quite expensive due to the small timesteps required to capture the fast Alfvén speeds in the very low- β coronae. To help mitigate this, which is made worse by the large density variation in such regions, in most simulations we also apply a density floor $\rho_{\text{fr}} = 10^{-4}\rho_0$, as used in previous works² (e.g., [Salvesen et al. 2016a](#); here ρ_0 is initial density maximum). Unfortunately, this density floor was found to have adversely affected some simulations by limiting the mean density profile far from the midplane. The issue occurs in the high- β states at lower H_{th} (see below), which are not our main focus in this work, because the thermal density profile involves an extremely sharp drop off away from the midplane (unlike the low- β states, which develop a much flatter power-law profile). In App. C we explicitly test the effect of changing the density floor on the low- β state, observing only tiny changes to mean profiles or transport rates.

In all simulations except those with net vertical flux, the mass loss over the duration of the simulation is mini-

mal. In the strongest NVF case with $\beta_z = 100$, we implement a mass replenishment by multiplying the density by a factor chosen to maintain constant total mass at every time step (as done in previous work; [Bai & Stone 2013](#)).

Note that, compared to previous works, we have run most simulations for a relatively short time (in units of Ω^{-1}). This is motivated by a desire to redeploy computational resources to explore finer resolutions (as needed for $\beta \ll 1$ and small H_{th}) and different simulations, rather than measuring precise values of α via long-time statistics. In support of this choice, we note that turbulence in stratified shearing boxes does not yet seem to be converged even at exceptionally fine resolution ([Ryan et al. 2017](#)), and detailed study along such lines is beyond the scope of this work. To ensure that the system is truly converged in time, we have run one simulation of the low- β state to beyond 100 orbits; this revealed a nearly constant statistical steady state with only small changes over long timescales.

3.4. Notation & Units

An average over the horizontal directions (x and y) is henceforth denoted by $\bar{f}(z) = A_\perp^{-1} \int dx dy f$ for any variable f with $A_\perp = L_x L_y$. A full volume average is $\langle f \rangle = A_\perp^{-1} L_z^{-1} \int dx dy dz f$, and an average over the thermal midplane is $\langle f \rangle_{\text{th}} = \frac{1}{2} A_\perp^{-1} H_{\text{th}}^{-1} \int_{-H_{\text{th}}}^{H_{\text{th}}} dx dy dz f$. These quantities are often also averaged over time after the initial transient phase in each simulation. ‘Fluctuations’ are denoted with a δ and defined as $\delta f \equiv f - \bar{f}$. The Alfvén speed is defined from the mean azimuthal field, which dominates all other mean components, as $v_A = \bar{B}_y / \sqrt{4\pi\rho}$, and β is defined as usual as the ratio of thermal to magnetic pressure (we average over x and y before taking their ratio). The dimensionless accretion stress is $\alpha = (\langle \rho u_x u_y \rangle - \langle B_x B_y \rangle) / \langle P_{\text{th}} \rangle$.

The shearing-box system is normalized to the arbitrary lengthscale L_0 , yielding freedom to define the simulation's units. To more clearly compare cases with strong magnetization, we do not normalize our box lengthscales to the thermal scale height H_{th} , unlike most previous works. Instead, in most simulations, because $H_\beta^2 = 2$ and $\beta < 1$, we have $H_{\text{th}} < 1$ in box units. However, everything in the system could, if desired, be rescaled to H_{th} , in which case our domain sizes would vary significantly between simulations and be much larger than $(L_x, L_y, L_z) = (10, 20, 10)$ (this would also rescale the density and velocity). Indeed, we find that small H_{th} (in box units) seems to be required to see the low- β state, which is equivalent to saying that very large domains $L_z \gtrsim 20$ are needed in thermal units. All plots and diagnostics are normalized to be dimensionless so can be meaningfully compared to previous works, showing good order-of-magnitude agreement where appropriate (see table 1).

4. THE PARKER AND MAGNETOROTATIONAL INSTABILITIES

Here we provide an overview of the magnetorotational and Parker instabilities ([Parker 1958](#); [Balbus & Hawley 1991](#)), which appear to be the primary linear instabilities driving the dynamics. While these instabilities and their relation to each other have been extensively explored in the literature (e.g., [Fogliizzo & Tagger 1995](#); [Balbus & Hawley 1998](#)) we focus here on the less-well-

² Another approach is to limit the Alfvén speed ([Johansen & Levin 2008](#)).

studied regime with $\beta \lesssim 1$ trans- or super-thermal magnetic fields, so it is helpful to collect and simplify some past results for more straightforward application to our simulations.

4.1. Magnetorotational instability

The MRI is driven by the energy in the background shear flow (unrelated to vertical stratification), and can be derived from Eqs. (1a) to (1c) by linearizing the equations near the midplane, dropping all z dependence. Assuming an equilibrium with constant azimuthal and vertical fields and no flows other than the background shear, we take solutions of the form $\delta f(\mathbf{x}) = \delta f \exp(ik_x x + ik_y y + ik_z z - i\omega t)$ in order to derive a dispersion relation for $\omega(\mathbf{k})$. Due to the background shear, k_x here should really be considered a function of time when k_y is non-zero (so called shearing waves with $k_z = k_{x0} + q\Omega k_y$; Johnson 2007; Lesur & Ogilvie 2008a; Squire & Bhattacharjee 2014) but we ignore this effect here, effectively considering mode growth over short timescales. The full dispersion relation is complicated, but by assuming $B_y \gg B_z$ (and $\omega \sim \Omega$) it simplifies to

$$\bar{\omega}^4 - \bar{\omega}^2 \left(4 - 2q + n^2 \frac{1+2x}{1+x} \right) + n^2(n^2 - 2q) \frac{x}{1+x} = 0, \quad (6)$$

where $\bar{\omega} = \omega/\Omega$, $n = (k_y v_{Ay} + k_z v_{Az})/\Omega$, and $x = c_s^2/v_{Ay}^2 \approx \beta$ following the notation of Begelman & Armitage (2023) (expanding (6) in $x \ll 1$ with $\bar{\omega} \sim x^{1/2}$ yields their equation (12) with $y = 0$). The full solutions to Eq. (6) are unhelpful, but can be expanded in various limits to yield simple results.

For high β ($x \gg 1$), Eq. (6) recovers standard MRI results, which are independent of v_{Ay} other than through n (Balbus & Hawley 1998): for $0 \leq q < 2$, ω is imaginary for $|n| < \sqrt{2q}$ (a purely growing mode), with $\text{Im}(\bar{\omega}) = n\sqrt{q}/(2-q)$ at $n \ll 1$ (long wavelengths) and a peak growth rate $\text{Im}(\bar{\omega}) = q/2$ at wavelength $n^2 = q - q^2/4$. For Keplerian rotation, $q = 3/2$, this yields $\text{Im}(\bar{\omega}) = 3/4$ at $n = \sqrt{15}/4$. At low β ($x \ll 1$) the shape of $\bar{\omega}(n)$ is very similar and it remains purely growing for $|n| < \sqrt{2q}$, but the growth rate decreases to $\text{Im}(\bar{\omega}) = n\sqrt{xq}/(2-q)$ at $n \ll 1$, giving $\text{Im}(\bar{\omega}) = \sqrt{3xn}$ at $q = 3/2$ (Begelman & Armitage 2023). Its peak growth rate shifts to $\text{Im}(\bar{\omega}) = \sqrt{2x}\sqrt{4-q-2\sqrt{4-2q}}$ at wavenumber $n^2 = 2(q-2+\sqrt{4-2q})$. For $q = 3/2$, these evaluate to $\text{Im}(\bar{\omega}) = \sqrt{x}$ at $n = 1$. With $q = 0$ (no shear) there is no instability, while with no rotation ($q \rightarrow \infty$ with $q\Omega = \text{const.}$) the growth rate peaks instead at $n = 0$ but scales as $\text{Im}(\omega) \propto 1/q$ (meaning it disappears in the non-rotating limit at both small and large β).

Overall, we see the only major change to the MRI with strong ($\beta \ll 1$) azimuthal fields is that the growth rate is suppressed by a factor $\sqrt{x} \approx \sqrt{\beta}$ compared to the $\beta > 1$ instability. This will presumably suppress the level of turbulence compared to the background magnetic field v_{Ay} at low β compared to the standard instability. The fastest growing MRI mode at $n \approx 1$ has azimuthal scale $k_y^{-1} \approx v_{Ay}/\Omega \sim H_{\text{th}}/\sqrt{\beta}$ so should be well resolved in our low- β simulations, which end up with $\beta \lesssim 1$ in the midplane (less so, perhaps, in the high- β simulations, if considering the mean-field β ; but for these our parameters are mostly similar to previous work, which exhibit well-known convergence issues; Ryan et al. 2017)

Also worth mentioning are other related, but fundamentally global instabilities at $\beta \ll 1$, which were first characterized by Pessah & Psaltis (2005) (the relevant dispersion relation was derived but left unexplored in Chandrasekhar 1961; see also Knobloch 1992; Gammie & Balbus 1994; Das et al. 2018). These instabilities are current driven, depending on the radial gradient of the (super-thermal) toroidal field,

$$\hat{B} \equiv \frac{d \ln B_\phi}{d \ln R}, \quad (7)$$

and reduce to the local MRI when $\hat{B} = -1$ such that $\mathbf{J} \propto \nabla \times (B_\phi \hat{\phi}) \approx 0$ (this point is not obvious in Pessah & Psaltis 2005, who set $\hat{B} = 0$). Begelman & Armitage (2023) give a simplified and more complete treatment, showing that their existence is controlled by the parameter $y \equiv (1 + \hat{B})^2 x^{-2} H_{\text{th}}^2 / R^2$, with a maximum growth rate that can be much faster than the standard low- β MRI when $y > 1$ and is not suppressed by $\sqrt{\beta}$ at low β . Of course, in the local simulations studied here, these instabilities do not exist, and we should thus think of the standard shearing box as being relevant only to the current-free case with $\hat{B} = -1$, in which case the global treatment reduces to the local one discussed above.

4.2. Parker instability

The Parker instability (Parker 1958) is driven by the vertical stratification of the magnetic field. Most commonly, it is studied while ignoring the effect of the radial shear; indeed, Shu (1974) argued that the instability cannot ever be fully stabilized by shear or rotation, because the growth rates of longer-wavelength modes can be suppressed and shear can play an important role by changing the radial wavenumber in time; Foglizzo & Tagger 1994, 1995). Convenient expressions are found in Goedbloed & Poedts (2004) Chapter 7, who consider a gravitating slab threaded by a perpendicular magnetic field $B_y(z)$ (without shear or rotation). Because the background equilibrium and gravitational acceleration $\hat{g} = -\Omega^2 z$ are z dependent, a correct treatment requires solving the boundary-value differential equation in z (Horiuchi et al. 1988); however, useful insight can be gained by considering local modes that vary rapidly over the length scale $L \sim z \sim B_y/B'_y$ on which the background varies (i.e., $\delta f \sim \exp(i\kappa z)$ with $\kappa L \gg 1$). This yields an effective local dispersion relation for $\omega(k_x, k_y, \kappa)$, which shows that two different types of modes can dominate the instability in different regimes: (i) the ‘‘pure interchange mode’’ with $k_{\parallel} = k_y = 0$, which does not bend the magnetic field, and (ii) the ‘‘quasi-interchange mode,’’ with $k_x \gg k_y$ but $k_y \neq 0$, which bends the field. We obtain simple expressions below by simplifying those of Goedbloed & Poedts (2004) assuming an isothermal equation of state, a $\beta \ll 1$ azimuthally directed mean field, and linear vertical gravity $\hat{g} = -\Omega^2 z$.³ In a true global disk, the vertical gravitational force and rotation change with

³ In the notation of Goedbloed & Poedts (2004), the disk atmosphere of interest becomes $\Gamma = -\hat{g} d \ln \rho / dz$, $\Gamma_B = c_s^{-2} \hat{g}^2$, $\Gamma_0 = c_s^{-2} \hat{g}^2 / (1 + 2/\beta)^2$, with $X^2 \equiv \Gamma / \Gamma_B$. The quasi-interchange dominates for $\Gamma_0 \leq \Gamma < \Gamma_B$ and the pure interchange dominates for $\Gamma \leq \Gamma_0$.

height far from the midplane; given our neglect of rotation and local treatment, the resultant modifications to the Parker instability can be captured by rescaling \hat{g} (Horiuchi et al. 1988).

Considering $z > 0$ regions with $d \ln \rho / dz < 0$ for concreteness, the general instability criterion becomes simply $dP_B/dz < 0$. Defining $X^2 \equiv |d \ln \rho / d \ln z| H_{\text{th}}^2 / 2z^2$, one finds quasi-interchange modes dominate when $X > \beta / (2 + \beta)$, while interchange modes dominate when $X < \beta / (2 + \beta)$. Noting that in low- β regions away from the midplane, $1 \gg \beta \propto z^{-2}$ while $|d \ln \rho / d \ln z| \sim \text{const.}$, we see that the quasi-interchange modes should dominate. Their maximum growth rate is,

$$\text{Im}(\omega) = \frac{\hat{g}}{v_A} (1 - X), \quad (8)$$

which, for the low- β power-law profile (4) is nearly constant with z because $v_A = c_s / \sqrt{2\beta} \propto z$ and $X \ll 1$ at $z \gg H_{\text{th}}$. Simplifying various expressions from Goedbloed & Poedts (2004), we find that the maximum growth rate occurs for parallel wavenumber

$$k_{\gamma, \text{max}} = \frac{\sqrt{2}z}{H_{\text{th}}} \frac{\Omega}{v_A} [(1 + \beta)X - (1 + \beta/2)X^2 - \beta/2]^{1/2} \\ \approx \left(\frac{a\sqrt{1 + a/2}}{zH_{\text{th}}} \right)^{1/2} \quad \text{for } z \gg H_{\text{th}}, \beta \ll 1, \quad (9)$$

where in the second line we used the power-law equilibrium (4), which fixes $v_A = \sqrt{2/a}\Omega z$. This applies at short radial length scales (there is no explicit dependence on k_x but shear and rotation affect small- k_x modes more) and small κ (large vertical length scales). Although the latter condition could be problematic for the local approximation, the growth rate becomes independent of κ for $\kappa \ll k_x$. This fastest-growing mode is captured by the azimuthal box size in our low- β simulations, since its lengthscale is smaller than z for $z \gg H_{\text{th}}$ ($k_y^{-1} \sim \sqrt{zH_{\text{th}}}$) and $L_y = 2L_z$ in most simulations.

5. RESULTS

5.1. Transition between the low- β and high- β states

The Gaussian initial conditions used for most simulations are in approximate vertical equilibrium but highly unstable to the Parker instability and MRI. The system thus rapidly reorganizes over the course of 2-3 orbits, transporting significant magnetic flux to larger z where it can escape out of the top and bottom boundaries, thereby organizing into a lower- β corona if the vertical domain is sufficiently large. During this reorganization phase, around half of the initial azimuthal magnetic flux is lost from the domain if starting from Gaussian initial conditions (this fraction seems to be independent of β), while for the quasi-Lorentzian initial conditions of Eq. (5) the fraction lost is lower because the initial state is rather similar to the final one. As per points 1-2 in §2, we find that two very different quasi-steady states result after it settles, the transition between which seems to be controlled by the midplane β following the transient reorganization phase. If too little flux remains after this phase, it all escapes. Alternatively, if the system remains sufficiently magnetized, the flux's escape is balanced by its regeneration and is maintained in steady state. For constant- β Gaussian initial conditions, we find that the

tipping point occurs for an initial $\beta \simeq 0.1$: higher- β initial conditions transition into the high- β state, lower- β ones transition into the low- β state, and those with $\beta = 0.1$ are sensitive to the details, as described below. Note, however, that this $\beta \simeq 0.1$ threshold is specific to the choice of the constant- β Gaussian: for the Lorentzian-like form (5), the system transitions into the low- β state from larger initial midplane β (e.g., ≈ 0.35 for $\beta 0.1$ -LorH) because the vertical equilibrium starts closer to its steady state structure.

We illustrate this transition in Fig. 2, which shows so-called ‘‘butterfly diagrams’’ of the time evolution of $\overline{\mathbf{B}}(z)$ (the x, y mean of \mathbf{B}). The top panels show cases that transition into the high- β state, which is characterized by dynamo cycles that quasi-periodically reverse the azimuthal field, in good agreement with previous work (Simon et al. 2012; Salvesen et al. 2016a). The three cases shown, $\beta 1$, $\beta 0.3$, and $\beta 0.1$ have the same initial H_β but successively decreasing initial β , and thus H_{th} , in the Gaussian initial conditions (Eq. (3)). Each case loses nearly all of its initial midplane magnetic flux to yield a thermally dominated midplane. The dynamo cycles are well formed and coherent, each with a similar period of $\simeq 10$ orbits, showing that the cycle period is independent of the sound speed (as expected since similar physics seems to occur in homogenous and/or incompressible models; e.g., Lesur & Ogilvie 2008b; Shi et al. 2016).

The lower panels show results initialized with more flux, which instead sustain the low- β state. The first, $\beta R 0.1$ is identical to $\beta 0.1$ except that it is also initialized with a mean radial field with $\beta_x = 100$ (the sign is such that $B_x B_y < 0$ as required to strengthen the initial B_y). The dynamics are very different to $\beta 0.1$ — there are no cycles and the system maintains a much stronger B_y in the midplane. Lower-initial- β simulations with smaller H_{th} ($\beta 0.05$ and $\beta 0.01$) reach a very similar state, albeit with a narrower midplane peak because this width is ultimately set by H_{th} (see below). Changes to \overline{B}_y in time are small amplitude, slow, and seemingly random. There also occurs times over which the midplane field strengthens, showing that these simulations are not simply taking longer to lose their flux. Initial conditions with $\beta = 0.1$ seem to lie on the boundary between reaching the low- and high- β states. This is evidenced by the fact that $\beta 0.1$ loses its flux significantly more slowly than $\beta 1$ and $\beta 0.3$, and a coarser-resolution version of the same setup ($\beta 0.1$ -mr) reaches the low- β state. This latter outcome appears to be a consequence of the expulsion of the flux being somewhat less efficient at coarser resolution: when initialized with an additional very weak ($\beta_x = 1000$) radial field that weakens the initial B_y (i.e., $B_x B_y > 0$), the same setup instead transitions into the high- β state (simulation $\beta nR 0.1$ -mr). The simulation $\beta 0.1$ -mr has been run over a significantly longer time, around 100 orbits, in order to test for sudden or long-term changes to the low- β state. Its lack of significant change over this time suggests that the system can maintain the low- β state indefinitely.

The dramatically different appearance of the low- and high- β states is illustrated in Fig. 3. The azimuthal field structure is very different: the high- β state is characterized by a super-Alfvénic midplane with $\delta \mathbf{B} \gg \overline{B}_y$ and small-scale fluctuations (their scale is likely resolution de-

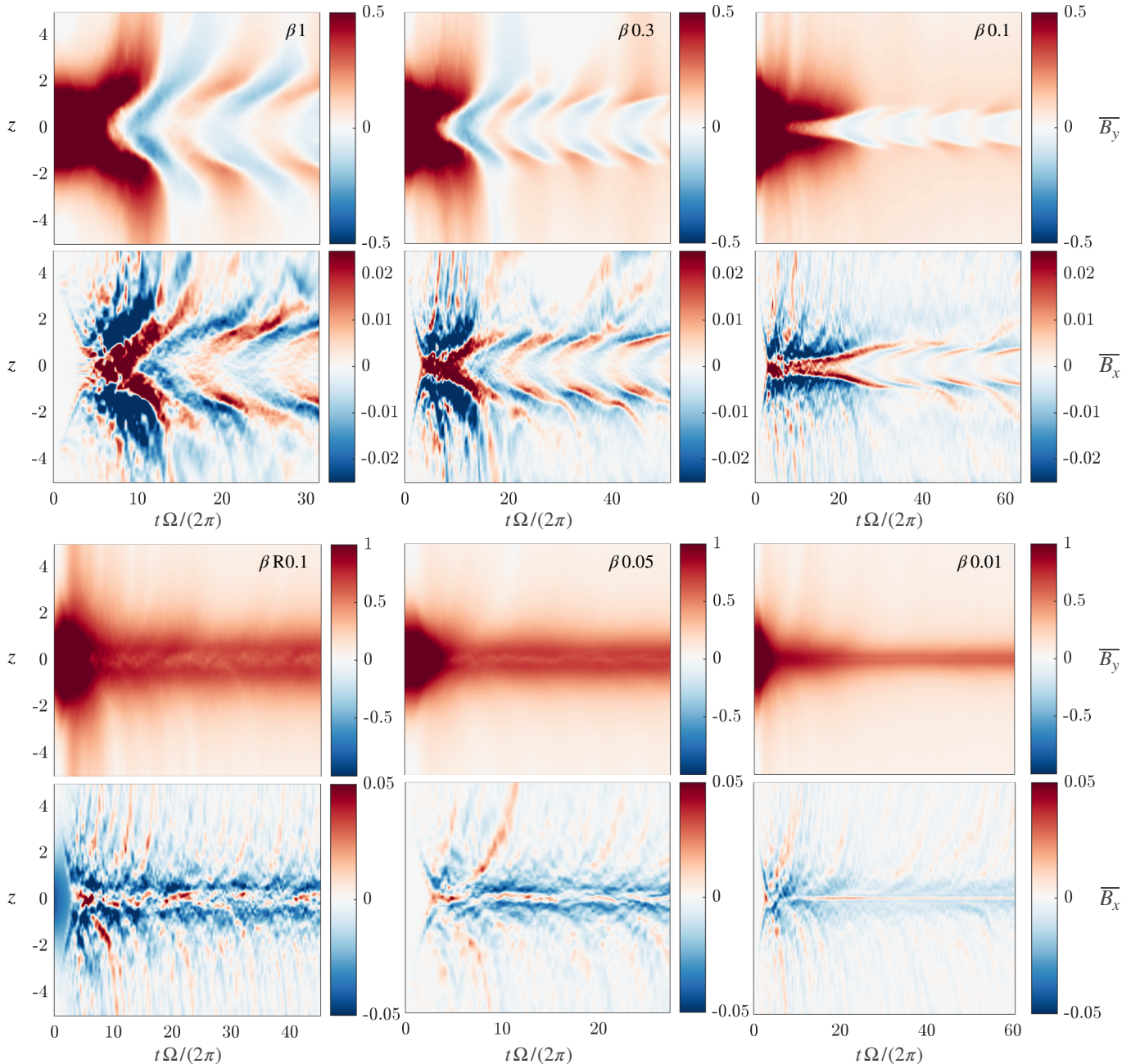


FIG. 2.— Space-time ‘butterfly’ plots for a range of ZNVF simulations with different initial conditions and sound speeds. Each case shows $\overline{B}_y(z, t)$ in the top subpanel and $\overline{B}_x(z, t)$ in the bottom subpanel. In the top row, we see cases that transition into the high- β weakly accreting state ($\beta 1$, $\beta 0.3$, and $\beta 0.1$) because they do not retain sufficient magnetic flux during their initial relaxation phase; these develop into well-studied dynamo cycles. The bottom panels show various cases that maintain the lower- β strongly accreting state ($\beta R0.1$, $\beta 0.05$, and $\beta 0.01$); these maintain a quasi-steady state with $\beta \lesssim 1$ in the midplane, losing significantly less flux through the boundaries during the initial phases and then maintaining a strong mean field in steady state.

pendent; see [Ryan et al. 2017](#)); the low- β state is mean-field dominated ($\delta \mathbf{B} < \overline{B}_y$) but clearly quite intermittent with small localized regions where the field reverses. Likewise, the density, which is much closer to perfectly thermal (Gaussian) in the high- β than the low- β state, looks very different, with much larger fluctuations in the midplane at low β because of its stronger turbulence. This also causes larger surface-density variation in the low- β state (see insets).

The aforementioned behavior is illustrated more quantitatively in Figs. 4 and 5, which show, respectively, time-

averaged density and magnetic-pressure profiles, and the time evolution of key quantities. The former shows how high- β profiles are thermally dominated out to $\simeq 2H_{\text{th}}$, with a lower- β corona above this (note that P_B here is defined using the mean fields as $P_B = \overline{B}_y^2 / 8\pi$ averaged over time; when fluctuations are also included in P_B , $\beta \approx 40$ in the midplane).⁴ The low- β state is magnet-

⁴ The mean density profile in all three cases shown here approaches the artificial density floor of 10^{-4} at the z boundaries. This may artificially flatten the density profile and, as a conse-

Name	β_{y0}	β_{x0}	β_z	$H_{\text{th}} = \sqrt{2} \frac{c_s}{\Omega}$	$N_x \times N_y \times N_z$	$(t_{\text{av}}, t_{\text{fin}}) \frac{\Omega}{2\pi}$	BCs	Notes	Outcome	$\langle \alpha \rangle$
$\beta 1$	1	∞	∞	1	448^3	(20,32)	Outflow		High- β	0.039
$\beta 0.3$	0.3	∞	∞	0.68	448^3	(20,52)	Outflow		High- β	0.029
$\beta 0.1$	0.1	∞	∞	0.43	448^3	(30,62)	Outflow		High- β	0.017
$\beta R 0.1$	0.1	100	∞	0.43	448^3	(10,45)	Outflow		Low- β	0.62
$\beta 0.1\text{-mr}$	0.1	∞	∞	0.43	336^3	(10,100)	Outflow		Low- β	0.49
$\beta n R 0.1\text{-mr}$	0.1	1000	∞	0.43	336^3	(30,64)	Outflow	$B_x B_y > 0$	High- β	< 0.02
$\beta 0.05$	0.05	∞	∞	0.31	448^3	(10,27)	Outflow		Low- β	0.57
$\beta 0.01$	0.01	∞	∞	0.14	336^3	(10,60)	Outflow	H_{th} marg. resolved	Low- β	0.61
$\beta 0.01\text{-hr}$	0.01	∞	∞	0.14	672^3	(4,8)	Outflow	Restart from $\beta 0.01$	Low- β	0.46
$\beta 0.001$	0.001	∞	∞	0.045	336^3	(10,18)	Outflow	H_{th} unresolved	Low- β	15
$\beta 0.1\text{-H4}$	0.012	∞	∞	0.43	336^3	(18,23)	Outflow		Low- β	0.35
$\beta 0.1\text{-LorH}$	≈ 0.35	∞	∞	0.43	336^3	(20,40)	Outflow	Eq. (5): $a = 3, H = 1$	Low- β	0.47
$\beta 0.1\text{-LorL}$	≈ 3	∞	∞	0.43	336^3	(30,42)	Outflow	Eq. (5): $a = 2, H = 0.45$	High- β	0.024
$\beta R 0.1\text{-S13}$	0.1	100	∞	0.43	336^3	(10,18)	Simon13		Low- β	0.81
$\beta R 0.1\text{-L13}$	0.1	100	∞	0.43	336^3	(10,19)	Lesur13		Low- β	0.64
$\beta R 0.1\text{-PL}$	0.1	100	∞	0.43	336^3	(10,20)	Power-law		Low- β	0.68
$\beta R 0.1\text{-rec2}$	0.1	100	∞	0.43	336^3	(10,14)	Power-law	HLLD 2 nd -order	Low- β	0.74
$\beta 0.1\text{-tall}$	0.1	∞	∞	0.43	$224^2 \times 336$	(15,27)	Outflow	$L_z = 7.5, \rho_{\text{flr}} = 10^{-9}$	Low- β	0.14
$\beta R 0.1\text{-NVF3}$	0.1	100	1000	0.43	336^3	(10,24)	Power-law		Low- β	0.75
$\beta R 0.1\text{-NVF2}$	0.1	100	100	0.43	336^3	(10,24)	Power-law	Density replenished	Low- β	2.1

TABLE 1

A LIST OF THE MAIN SIMULATIONS ANALYZED IN THIS WORK WITH RELEVANT PARAMETERS, INITIAL CONDITIONS, AND OTHER PROPERTIES. THE SIMULATION NAME IS CHOSEN BASED ON THE INITIAL β IN A GAUSSIAN EQUILIBRIUM (3) WITH $H_\beta = \sqrt{2}$, THUS EFFECTIVELY PROVIDING A CORRESPONDENCE WITH THE THERMAL SCALE HEIGHT IN BOX UNITS (COLUMN 4). THE SEVENTH COLUMN LISTS THE FINAL TIME AND THE “STEADY STATE” TIME t_{av} , WITH AVERAGES PERFORMED FOR $t \in (t_{\text{av}}, t_{\text{fin}})$. BOUNDARY CONDITIONS (“BCS”) ARE DESCRIBED IN §3.2. “OUTCOME” LISTS WHETHER THE SIMULATION REACHES THE LOW- OR HIGH- β STATE, WHICH IS DETERMINED BY ITS TIME-AVERAGED PROFILE AND α (FINAL COLUMN). OTHER SIMULATIONS USED FOR NUMERICAL TESTS ARE LISTED IN TABLE 2.

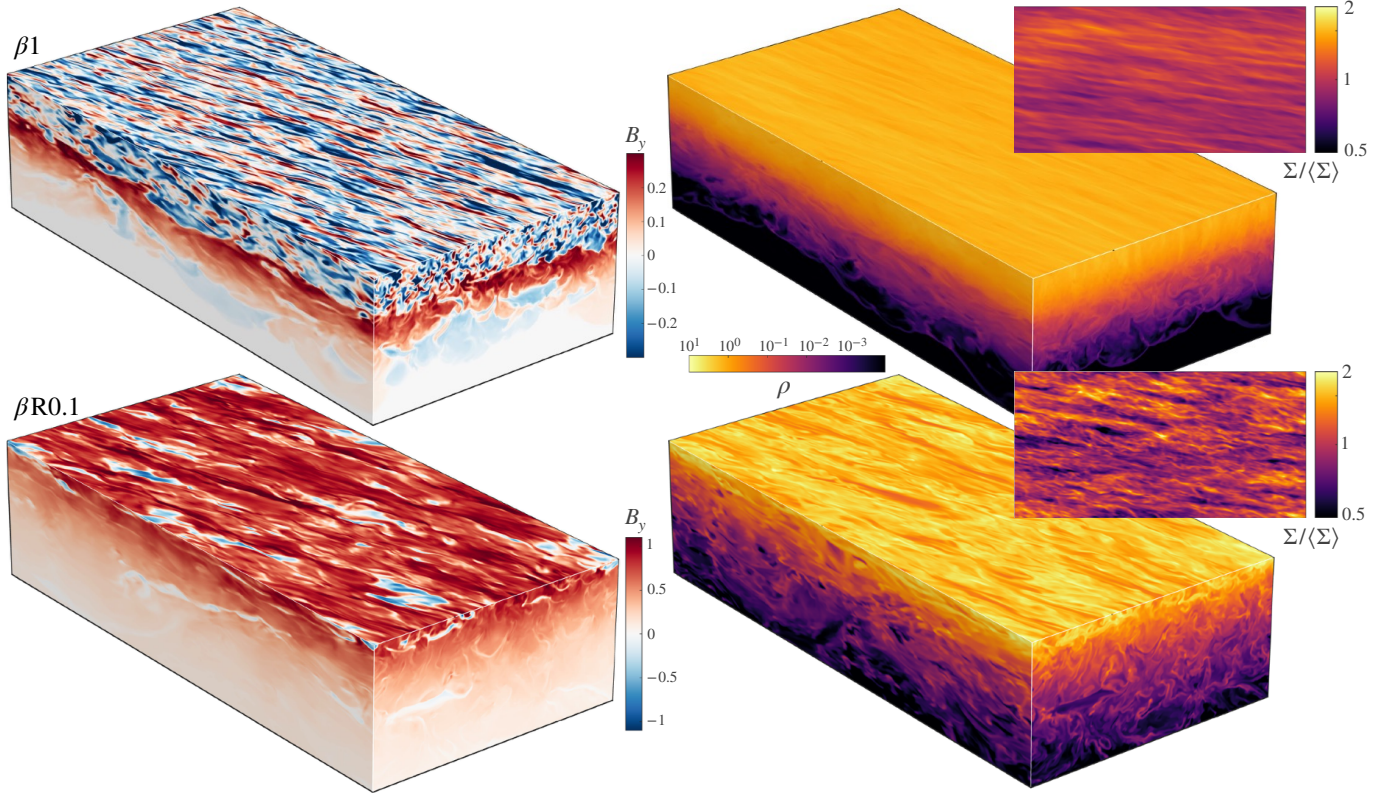


FIG. 3.— Azimuthal-field (left) and density (right) snapshots from the quasi-steady state ($t\Omega/2\pi \approx 30$) of $\beta 1$ in the high- β state (top panels) and $\beta R 0.1$ in the low- β state (bottom panels). Each 3-D rendering shows just the bottom half of the domain to illustrate the midplane structure, and the inset on the right-hand panels shows the surface-density fluctuations ($\Sigma \equiv \int dz \rho$). The structures are very different between the two states, with significantly larger fluctuations in density in the low- β state due to its more vigorous turbulence.

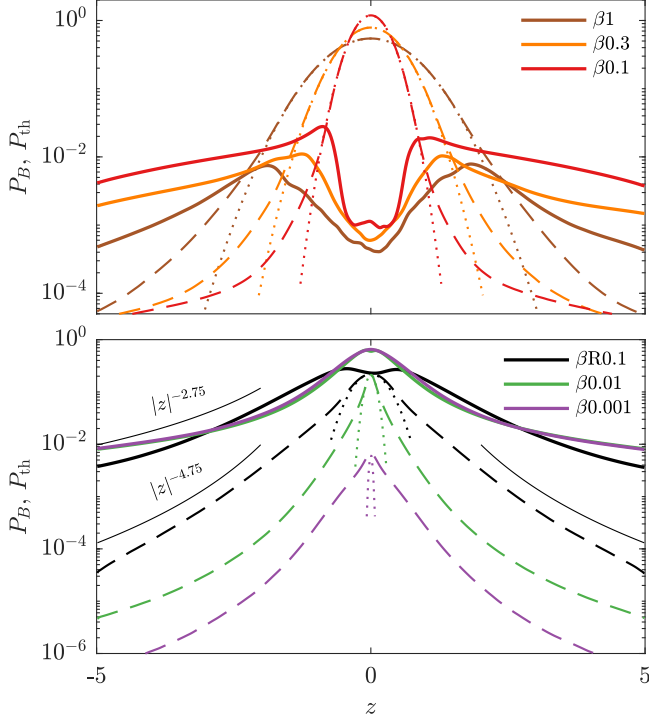


FIG. 4.— In each panel, solid lines show the average-field magnetic pressure $P_B = \overline{B_y^2}/8\pi$ and dashed lines show the thermal pressure $P_{\text{th}} = c_s^2 \overline{\rho}$, each averaged over the quasi-steady state. In the top panel, we show simulations that reach the high- β cycles (with the time average taken over these high- β cycles); in the bottom panel we show several that reach the low- β state. In each case, the dotted line shows the thermal solution, $\rho \propto \exp(-z^2/H_{\text{th}}^2)$ and the total normalization is such that $\int dz (P_{\text{th}} + P_B) = 1$.

ically dominated everywhere, though increasingly so at large z , where the profiles are approximate power laws with an index $a \approx 2.75$ in Eq. (4). The lowest- β initial conditions ($\beta 0.01$ and $\beta 0.001$) also retain $\beta \ll 1$ midplanes in steady state, although we argue below that this is likely a consequence of not adequately resolving H_{th} , which sets the shape of ρ for $z \lesssim H_{\text{th}}$ (see dotted lines for $\beta R0.1$). The small dip in P_B in the midplane is a persistent feature when properly resolved; this is a consequence of the pressure support being thermal rather than magnetic at the midplane and also implies that the Parker instability is quenched there since $z dP_B/dz > 0$. By solving Eq. (2) for $\overline{B_y}$ from the measured $\overline{\rho}$, then comparing this to the measured $\overline{B_y}$ (or vice versa from $\overline{B_y}$ to $\overline{\rho}$), we find that the mean low- β profiles in Fig. 4 are almost exactly equilibria (not shown). This is expected because the turbulence remains sub-Alfvénic, justifying directly the magneto-static approach of §3.1.

Figure 5 shows the time evolution of the total accretion stress $\alpha \equiv (\langle \rho u_x u_y \rangle - \langle B_x B_y \rangle) / \langle P_{\text{th}} \rangle$, the midplane β including fluctuations ($\beta_{\text{mid}} \equiv 8\pi c_s^2 \langle \rho \rangle_{\text{th}} / \langle B^2 \rangle_{\text{th}}$), and the midplane $\overline{B_y}$ for the simulations shown in Fig. 2 as well as several other illustrative examples. Most importantly, we see a large “gap” between the low- β and high- β states for each quantity. As well as clearly illustrating the bimodality in β between the two states, these show

quence, P_B at large z , thus also reducing high- z turbulent fluctuations due to the weaker Parker instability.

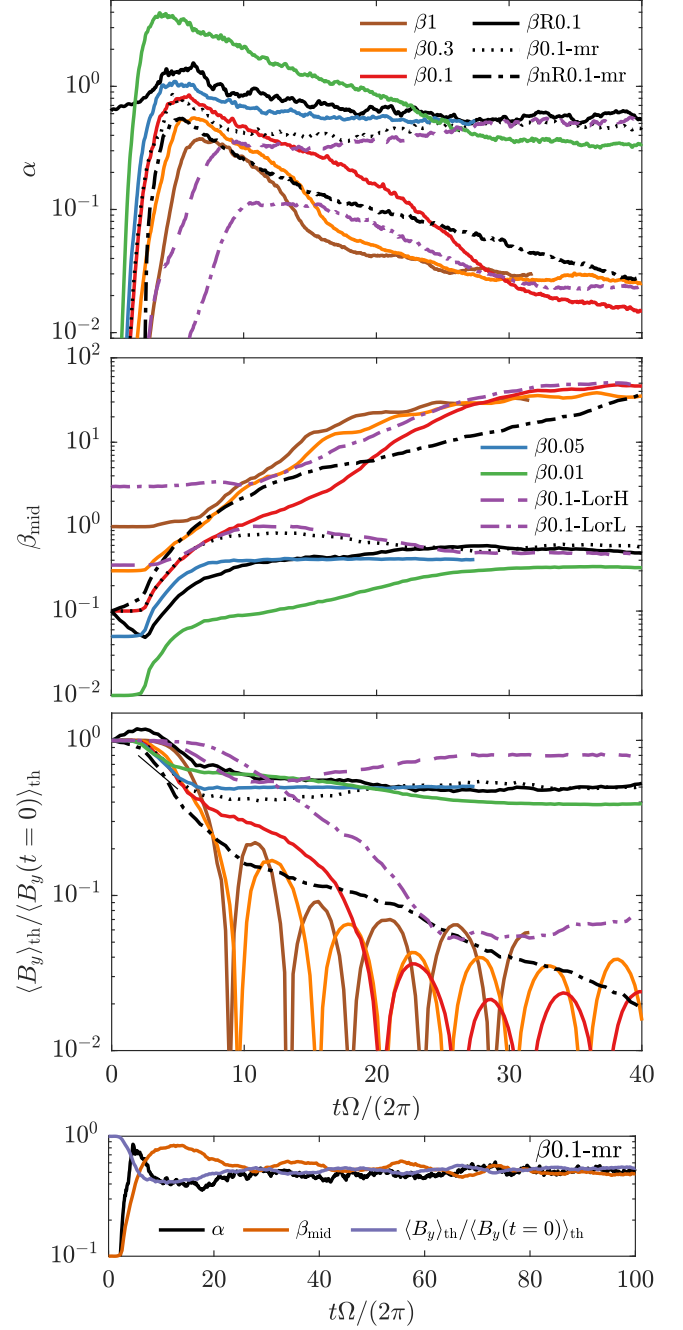


FIG. 5.— Time evolution of various important quantities from the simulations shown in Fig. 2, as well as several others that illustrate important features. The top panel shows the total accretion stress $\alpha = (\langle \rho u_x u_y \rangle - \langle B_x B_y \rangle) / \langle P_{\text{th}} \rangle$, and the second and third panels show the midplane β and magnetic flux $\langle B_y \rangle_{\text{th}} / \langle B_y(t=0) \rangle_{\text{th}}$, respectively, where the midplane is defined here as the region $|z| \leq H_{\text{th}}$ (the thin black line on $\langle B_y \rangle_{\text{th}} / \langle B_y(t=0) \rangle_{\text{th}}$ shows $2\pi\Omega^{-1} d \ln \langle B_y \rangle_{\text{th}} / dt \approx 1/6$ for later discussion). We see clearly bimodal behavior in all quantities for various initial conditions and resolutions, although which state it reaches can have dependence on numerical parameters for cases near the transition (cf. $\beta 0.1$ and $\beta 0.1\text{-mr}$). The initial β_{mid} is higher for the cases starting from Lorentzian-like initial conditions because this equilibrium already has a strongly magnetized corona at larger z . The bottom panel shows the same quantities for $\beta 0.1\text{-mr}$ over its full time duration of ≈ 100 orbits. We do not observe any long-term or sudden changes to the low- β state.

more concretely that (i) the low- β state supports much higher accretion rates and (ii) the low- β state retains much more of the midplane magnetic flux from the initial conditions, whereas nearly all of the flux ($\gtrsim 95\%$) is lost in the evolution towards the high- β state. It also highlights how the $\beta = 0.1$, $H_\beta = \sqrt{2}$ initial conditions ($\beta 0.1$, $\beta R0.1$, $\beta 0.1\text{-mr}$, and $\beta nR0.1\text{-mr}$) are sensitive to slight changes in resolution and initial conditions: $\beta 0.1$ transitions to the high- β state rather slowly, while $\beta R0.1$ stays at low β due to the extra contribution from B_x that initially strengthens B_y ($B_x B_y < 0$); $\beta 0.1\text{-mr}$ (at coarser resolution) evolves back to lower β and higher α after initially evolving similarly to $\beta 0.1$, but adding a very weak radial field with $B_x B_y > 0$ such that B_y is initially made weaker ($\beta nR0.1\text{-mr}$) causes it to transition to the high- β state (note that this B_r with $\beta_x = 1000$, is weaker than that which occurs self-consistently in the low- β saturated state). We also show two cases that start instead from the quasi-Lorentzian initial conditions of Eq. (5). Because these profiles are already magnetically dominated at large z , they evolve less violently over the initial phases. Nonetheless, the bimodal behavior persists, with the lower- β initial condition maintaining the strongly magnetized state and \overline{B}_y increasing, while the higher- β initial condition loses nearly all of its midplane flux.⁵

The bottom panel of Fig. 5 shows the evolution of the same three quantities for the longest-run simulation ($\beta 0.1\text{-mr}$). After its initial dip in α (described above), the system remains remarkably steady, other than low-amplitude, slow ($\simeq 20$ orbit-period) oscillations in the field and β_{mid} . Importantly, there is no evidence for the system transitioning out of the low- β state once it is reached, although we obviously cannot rule out the possibility that this could occur over longer timescales.

5.2. Turbulence and transport at low β

The turbulence profiles in the low- β state are shown in Figs. 6 and 7. Figure 6 shows $\overline{\alpha}(z)$ in $\beta R0.1$ and $\beta 1$, splitting the total into its contributions from velocity $\alpha_K \equiv \overline{\rho u_x u_y} / \langle P_{\text{th}} \rangle_{\text{th}}$, magnetic fluctuations $\alpha_{\delta B} = -\overline{\delta B_x \delta B_y} / \langle P_{\text{th}} \rangle_{\text{th}}$, and the mean magnetic field $\alpha_{\overline{B}} = -\overline{B_x B_y} / \langle P_{\text{th}} \rangle_{\text{th}}$. The total $\overline{\alpha}(z)$ profile is similar to that of the equilibrium-field P_B (dotted line), aside from in the midplane, where there is a peak in the turbulent contributions and a drop off in the mean contribution. We interpret this change within $|z| \lesssim H_{\text{th}}$ as a result of the MRI becoming dominant, whereas the Parker instability prevails at larger z . This interpretation is supported by the similar ratios between the α components in the best-resolved high- β simulation ($\beta 1$), where the MRI remains active across a broad midplane region (cf. lower panel). We see that both MRI- and Parker-driven turbulence enable accretion ($\alpha > 0$), but the MRI-driven midplane regions have a stronger relative contribution from magnetic, compared to velocity fluctuations.

Figure 7 compares the time-averaged fluctuation amplitudes between $\beta R0.1$ (low- β ; black) and $\beta 0.1$ (high- β ;

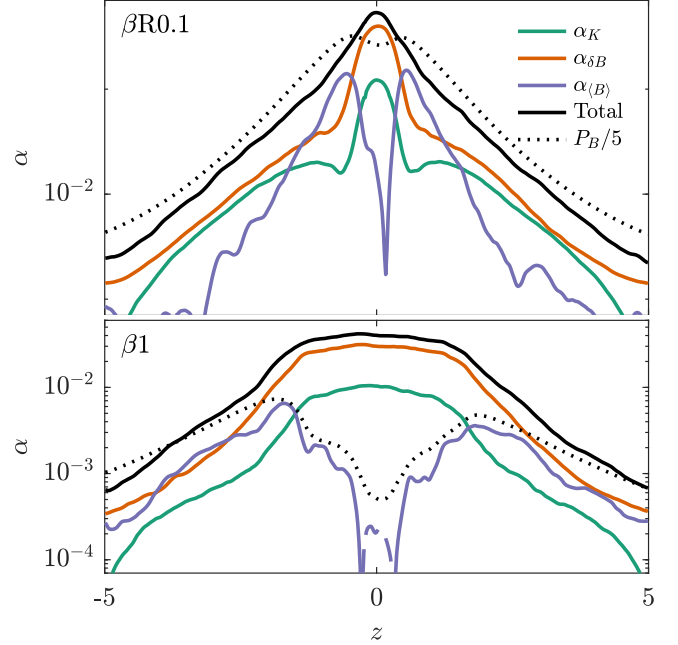


FIG. 6.— Spatial profile of the various components of the accretion stress in the low- β state ($\beta R0.1$; top) and the high- β state ($\beta 1$; bottom). We split $\alpha(z)$ into $\alpha_K \equiv \overline{u_x u_y}$, $\alpha_{\delta B} = -\overline{\delta B_x \delta B_y}$, and $\alpha_{\overline{B}} = -\overline{B_x B_y}$, each normalized by $\langle \rho \rangle_{\text{th}} c_s^2$. Magnetic contributions are dominant, with the total stress following a similar profile to P_B except right in the midplane.

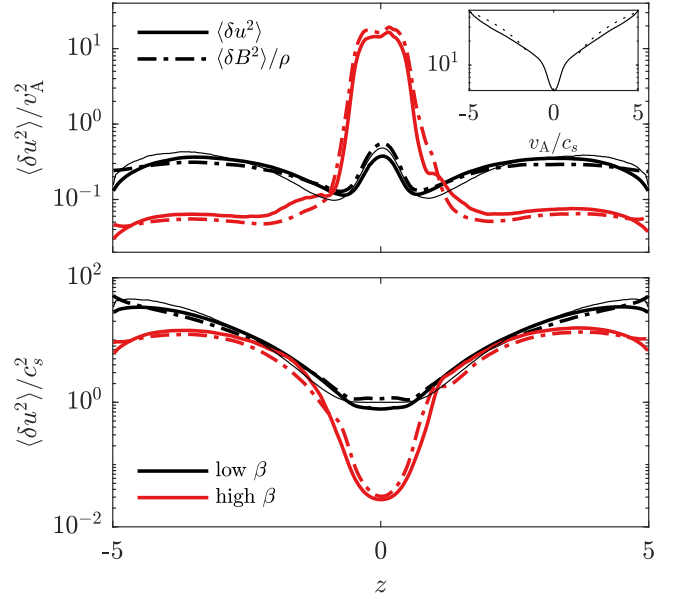


FIG. 7.— Comparison of the turbulence fluctuation profiles in the low- β state ($\beta R0.1$; black) and the high- β state at otherwise identical parameters ($\beta 0.1$; red). The top panel normalizes to the local Alfvén speed $v_A = \overline{B_y} / \sqrt{4\pi\overline{\rho}}$; the bottom panel normalizes to c_s . The thin black line shows a simple model of MRI & Parker instability driven turbulence (see text), and the top-panel inset shows the $v_A(z)$ profile with αz shown in dotted lines.

⁵ At 336^3 resolution and $H_{\text{th}} = 0.43$, the high- β state only sometimes produces well-formed cyclic behavior. Given the coarse effective resolution of the thermal midplane, and previous results documenting the resolution and box-size dependence of MRI turbulence (e.g., Davis et al. 2010; Ryan et al. 2017), this is not unexpected.

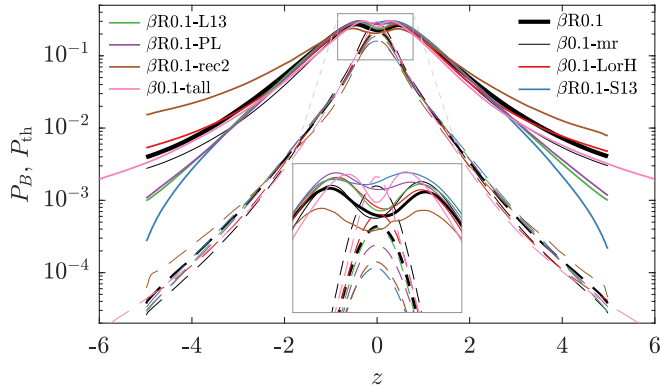


FIG. 8.— Testing different vertical boundary conditions, numerical options, and initial conditions (see table 1). As in Fig. 4, solid lines show P_B and dashed lines show P_{th} . The inset zooms into the midplane region.

red), normalizing by either the local mean v_A (top) or c_s (bottom). The low- β state exhibits trans-Alfvénic turbulence across its full profile with $\delta u^2 \simeq \delta B^2 / \bar{\rho} \approx 0.3v_A$, which is similar to that observed in H+24. This also implies the turbulence is highly supersonic at larger z with $\mathcal{M} = \delta u / c_s \gtrsim 10$.

The thin black line in both panels illustrates a simple model of the turbulence, based on driving by a combination of the MRI and Parker instability (see also Johansen & Levin 2008). For both instabilities, we apply the standard reasoning that the turbulence saturates when the nonlinear turnover time $\tau_{\text{nl}} \sim \ell / \delta u$ at the outer scale ℓ balances the instability’s growth rate. In regions far above the midplane, where the profiles of B_y , ρ , and v_A are all power laws, it is most natural to take $\ell \propto z$, such that the turbulence remains self-similar with z . Another possible choice, the lengthscale of the fastest growing mode, would scale in the same way for both the Parker and MRI: for Parker because it grows fastest at the largest available vertical scales (the global scales, $\propto z$), and for MRI because it grows fastest where $n \sim \Omega^{-1}v_A / \ell \sim 1$ and $v_A \propto z$ in such regions (see §3.1 and inset of Fig. 7).⁶ In contrast, near the midplane, since the shape of ρ is set by H_{th} , we require $\ell \lesssim H_{\text{th}}$. The Parker instability will not operate here because B_y is nearly flat, while the scale at which the MRI growth rate peaks ($n \approx 1$ in Eq. (6) with $v_A \sim c_s$) is $\ell \sim v_A / \Omega \sim H_{\text{th}}$, suggesting $\ell \sim H_{\text{th}}$ is a reasonable choice (this is also plausibly consistent with the morphology seen in Fig. 3 for $\beta\text{R0.1}$).

Combining these estimates for ℓ with the growth rates, for the MRI we have $\gamma \sim \sqrt{\beta}\Omega$ at $\beta \lesssim 1$, giving $\delta u \sim H_{\text{th}}\Omega \sim c_s$ in the midplane, and $\delta u \sim z\sqrt{\beta}\Omega \sim$

⁶ Similar arguments applied to the high- β state would suggest that we should take $\ell \sim v_A / \Omega$ of the fastest growing mode as the outer scale, where the v_A is that of the self-induced mean azimuthal field that can drive the MRI. This scale is very small, around $\ell \sim 4 \times 10^{-2} H_{\text{th}}$ for the $\beta 1$ simulation (effectively the grid scale), in reasonable agreement with the morphology seen in Fig. 3. If ℓ is indeed grid limited, then since $\delta u \propto \ell$ (assuming nearly constant growth rate), we would expect the turbulence amplitude to decrease with finer resolution (complicated, perhaps, by the fact that \bar{v}_A may itself depend on δu). This is consistent with the results of Ryan et al. (2017) who found that the turbulence decreased its amplitude and scale with finer resolution in the high- β state, even at extremely fine resolutions.

$c_s z \Omega / v_A \sim c_s$ for $z \gg H_{\text{th}}$ (using $v_A^2 \approx 2\Omega^2 z^2 / a$). We thus assume that the MRI contributes approximately trans-sonic turbulence $\delta u^2 \approx c_s^2$ at all z . For the Parker instability contribution, we compute the maximum growth rate directly from Eq. (8) based on the measured \bar{B}_y and $\bar{\rho}$, then fix $\ell \propto z$ with proportionality coefficient 0.4 chosen to fit the data. Adding these contributions leads to the thin black lines in Fig. 7, which provide an excellent match to the measured turbulence. The same prescription, with the same 0.4 coefficient, works well for the other low- β ZNVF simulations.

5.3. The effect of boundary conditions and numerical options

In Fig. 8 we illustrate the effect of changing the vertical boundary conditions and other numerical options on the low- β state. As listed in table 1, these simulations explore 4 different vertical boundary conditions based on previous literature (see §3.2), different initial conditions (Eq. (5)), a taller box with $L_z = 15$, and second-order reconstruction with an HLLD Reimman solver, but otherwise have the same parameters (e.g., c_s). They all reach a quasi-steady low- β state and we plot the steady-state time average of $P_B = \bar{B}_y$ and $P_{\text{th}} = c_s^2 \bar{\rho}$. Overall, we see that the general form is maintained for all cases, although there are certainly differences. Unsurprisingly, given that Simon13 boundary conditions fix the gradients of B_x and B_y to be large and negative at the boundary, these lead to the steepest P_B profile at larger z , while the Outflow boundaries, which set $B'_x = B'_y = 0$, do the opposite (the Lesur13 and Power-Law cases lie between these limits). Less obvious, however, is that these steeper P_B profiles lead to states that are more strongly magnetized (a lower- β midplane) with larger accretion rates α (see table 1), even though naively one might expect that carrying the flux out of the domain more efficiently would lead to lower midplane magnetic fields. Using 2nd-order reconstruction leads to the flattest profiles in P_B and ρ , which appears to be a consequence of it supporting modestly less vigorous turbulence at large z , and thus transporting the flux out of the midplane less efficiently. Finally, $\beta 0.1$ -tall — with an extended vertical domain (the full extent is not shown), fewer grid cells per H_{th} , and a much lower density floor — produces similar vertical profiles, albeit with lower midplane turbulence levels, which lead to lower α and larger β_{mid} . This difference is at least partially a consequence of its coarser resolution per H_{th} (see App. B), perhaps also influenced by its different domain aspect ratio (see App. A; other than the initial conditions, this case is equivalent to rescaling the vertical box to a lower H_{th} , as for $\beta 0.05$ or $\beta 0.01$).

Various other numerical tests are presented in the Appendices, which describe the dependence on domain aspect ratio (App. A), resolution (App. B), and the density floor (App. C). We briefly summarize these results here. We find that the azimuthal length of the box can have an important influence, with $\beta = 0.1$ initial conditions that transition to the low- β state in a longer box instead transitioning to the high- β state in a shorter box. We interpret this behavior as relating to the Parker instability, which seems to be needed to regenerate the field against vertical escape. The fastest growing Parker-instability modes in this regime are of the “quasi-interchange” variety, which have a specific azimuthal scale (9) that ap-

proaches the box scale with shorter boxes, thus potentially interfering with the turbulence. The radial box size does not appear to have an important influence. The dependence on resolution is interestingly non-monotonic, with the transport decreasing with coarsening resolution until 1-2 zones per H_{th} , then suddenly increasing dramatically at yet coarser resolutions. This behavior arises because the turbulence in the midplane is suppressed with coarser resolution, thus reducing the transport for similar profiles; but, once the resolution drops so low that it acts to support the collapse of density to the thermal profile in the midplane, the system no longer loses its magnetic flux and supports a $\beta \ll 1$ midplane with higher transport (see §5.5 and e.g., $\beta 0.001$ in Fig. 4). Several direct tests show effectively no dependence of the low- β state on the choice of density floor. Finally, in App. D we demonstrate that both shear and rotation are required to maintain the low- β state. Interestingly, in the absence of rotation the system still exhibits high- β dynamo cycles; since the MRI does not exist in this case (see §4.1), this suggests that the cyclic dynamo is not associated with the MRI, as usually assumed.

A final numerical issue worth discussing is that the low- β state requires a large separation between the vertical domain size and H_{th} . This conclusion is based on test simulations at the same H_{th} as $\beta 1$ or $\beta 0.3$, but with either a stronger initial magnetic field with $\beta < 0.1$ (and thus a larger H_β) or with initial radial flux that is sheared into an azimuthal field in the simulation’s early stages (as in e.g., $\beta\text{R0.1}$). These tests lose their flux and transition into the high- β state. The same behavior occurs at resolutions with fewer zones per H_{th} than some low- β simulations (e.g., $\beta\text{R0.1}$), showing that it is not an indirect consequence of changing the resolution per H_{th} . This suggests that the low- β state can be maintained only when there exists an extended strongly magnetized corona, perhaps because the Parker-driven dynamo requires an atmosphere of sufficient vertical extent and/or due to direct effects from the boundary conditions.

Overall, we see that while numerical options do have an important impact on the results, as is also the case for the high- β shearing-box turbulence (e.g., Guan et al. 2009; Gressel 2013; Ryan et al. 2017), the general features of the low- β state seem robust.

5.4. The effect of vertical flux

Previous works have found that strongly magnetized ($\beta < 1$) profiles are sustained in the presence of a net vertical flux threading the box (e.g., Suzuki & Inutsuka 2009; Bai & Stone 2013). We explore here how the ZNVF low- β state changes with β_z , finding that it smoothly transitions into this low- β NVF state as β_z decreases below $\beta_z \simeq 10^3$. The general shape of the profiles remains rather similar as this occurs. In other words, while for $\beta_z \gtrsim 10^3$ there exist two qualitatively different self-sustaining accretion states depending on the initial toroidal flux threading the system, for $\beta_z \lesssim 10^3$ the system always reaches a strongly accreting state characterized by a $\beta \lesssim 1$ midplane, wider density profiles, and a lack of dynamo cycles (much longer-time-duration simulations are shown in Bai & Stone 2013; Salvesen et al. 2016b with Salvesen et al. 2016b’s exhibiting widely spaced, aperiodic flips in polarity at $\beta_z = 100$). However, as argued in §6 below, despite the similar appearance of

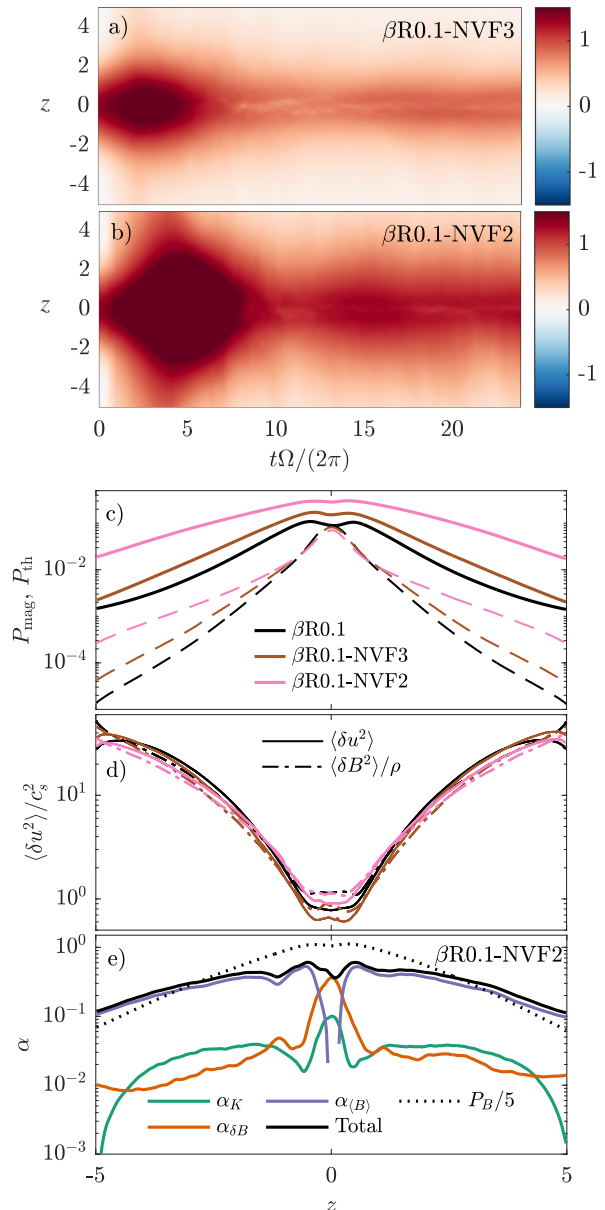


FIG. 9.— The effect of a net vertical flux on the low- β state. Panels a and b show butterfly diagrams of $\overline{B_y}$ (cf. Fig. 2) starting from the same initial conditions as $\beta\text{R0.1}$, but with a net vertical flux of $\beta_z = 1000$ or $\beta_z = 100$. Diagnostics of the vertical equilibrium (cf. Fig. 4) and turbulence (cf. Fig. 7) are shown in panels c and d, respectively, while panel e shows the contributions to α for the $\beta_z = 100$ case (cf. Fig. 6). The $\beta_z = 1000$ field makes little noticeable difference to the morphology, raising α slightly, while $\beta_z = 100$ causes a stronger mean field, lowering the midplane β , in line with previous results (Suzuki & Inutsuka 2009; Bai & Stone 2013; Salvesen et al. 2016b).

the ZNVF and NVF states, the mechanism that sustains the strong azimuthal field with NVF is very different: NVF drives a single large-scale MRI channel mode, while the ZNVF state is supported by the turbulent dynamo.

Our results are collected in Fig. 9. In the top panel we show butterfly diagrams for the same setup as $\beta\text{R0.1}$ but with $\beta_z = 10^3$ (panel a) and $\beta_z = 100$ (panel b). The profiles and time evolution appear similar to Bai & Stone (2013); Salvesen et al. (2016b), as well as those with ZNVF (cf. Fig. 2), although with $\beta_z = 100$ the

field becomes significantly stronger and less peaked in the midplane after its initial phase (see also the quasi-steady-state profiles in Fig. 9c). The accretion rate α is also higher at $\beta_z = 100$ ($\langle\alpha\rangle \approx 2.1$ at $\beta_z = 100$, versus $\langle\alpha\rangle \approx 0.7$ and $\langle\alpha\rangle \approx 0.6$ for $\beta_z = 10^3$ and $\beta_z = \infty$, respectively).⁷ This larger $\langle\alpha\rangle$ at lower β_z is not a consequence of the turbulent fluctuations, which are hardly stronger at $\beta_z = 100$ than at $\beta_z = \infty$ (see panel d); instead its accretion stress is nearly flat with z and almost entirely due to the mean field $-\overline{B_x B_y}$ (see panel e). This agrees with the conclusions of Bai & Stone 2013 (see their figure 6). This behavior results from $\overline{B_x}$ being generated from $\overline{B_y}$ via direct stretching of the net vertical field (as opposed to via the turbulence in ZNVF simulations): this more efficient feedback, which is effectively the aforementioned domain-scale MRI channel mode, increases α and lowers β due to the stronger fields (see §6). As in previous works, we also observe much stronger outflows at $\beta_z \lesssim 10^3$, which cause significant mass loss over time if the density is not continuously replenished via the artificial source term. Despite the lower β at $\beta_z = 100$, the density still collapses towards the thermal scale height within $|z| \lesssim H_{\text{th}}$, with a similar midplane density structure as the ZNVF runs.

5.5. Collapse towards the $\beta \simeq 1$ midplane

Figures 4 & 5 show that even when ZNVF simulations are initialized with $\beta \ll 1$ and reach the low- β state, the midplane usually reaches a gas-pressure dominated $\beta \sim 1$ steady state. Here we explore how the system behaves as it loses magnetic flux and evolves towards a $\beta \sim 1$ midplane, also showing that the process is sensitive to resolving the thermal scale height.

Figure 10 shows several numerical experiments that probe this physics, illustrating the time evolution of P_{th} and P_B . The top panel shows a simulation ($\beta 0.1$ -H4) with the same H_{th} and box size as $\beta\text{R}0.1$ or $\beta 0.1$ -mr, but with a more strongly magnetized initial condition with $\beta \approx 0.01$. It thus starts with a wider profile with $H_\beta \approx 4$, effectively simulating the small central patch $|z| \lesssim 1.6$ of $\beta 0.01$ (L_x and L_y would also be similarly scaled). After a short reorganization phase from the Gaussian initial conditions, the system settles into a quasi-equilibrium state with P_B flatter than P_{th} , similar to the central region of the generalized power-law profile Eq. (5) (see Fig. 1). This strong field then escapes through the boundary over $\simeq 15$ orbits, with the density becoming more peaked and P_B developing its characteristic “dip” at $z = 0$, before halting and reaching steady state at $\beta \sim 1$ (cf. Fig. 8). The same behaviour is observed for $\beta 0.05$ (middle panel) and other simulations (not shown), albeit with a shorter field-decrease phase because they start from higher β initially. In fact, the measured rate of field decrease over this phase, $2\pi\Omega^{-1} d \ln B_y / dt \approx 1/6$, seems to be independent of boundary conditions, β , or resolution, as indicated by the thin black line in the lower panel of Fig. 5. This might be expected for Parker-instability-driven turbulence given its β -independent growth rate $\gamma \sim \Omega$ (see

⁷ Salvesen et al. (2016b) and Bai & Stone (2013) report $\langle\alpha\rangle \simeq 1.0$ at $\beta_z = 100$ when measured at the midplane or $\langle\alpha\rangle \simeq 1.5$ when measured over the full profile. The larger $\langle\alpha\rangle$ we report here is due to the larger L_z/H_{th} in our simulation, since $\langle\alpha\rangle$ is normalized by $\langle\rho\rangle$ and $\bar{\rho}$ decreases more rapidly with z than $\overline{B_x B_y}$ (see Fig. 9f).

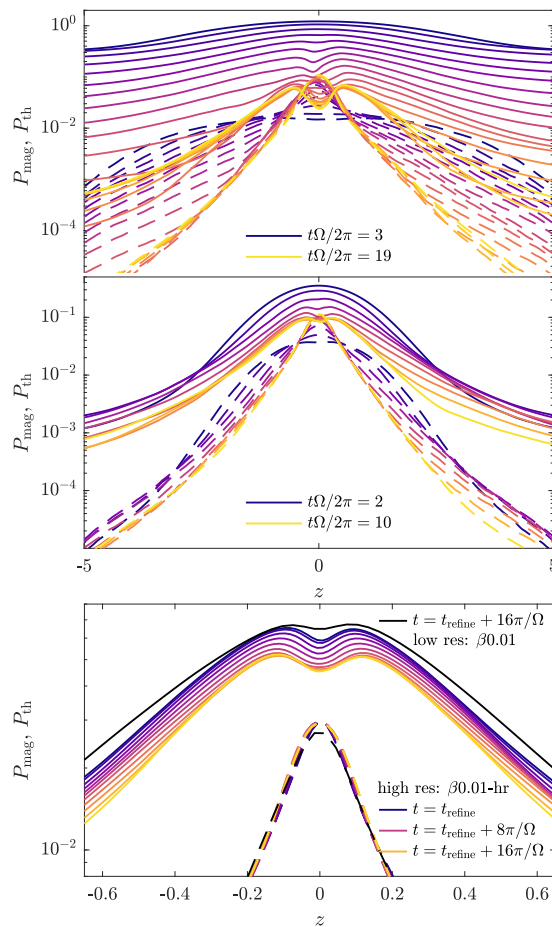


FIG. 10.— Magnetic and thermal pressures (as in Fig. 4) as a function of time, from dark purple to yellow in equal time increments of approximately 1 orbit, over the time range indicated on each panel. The top panel shows $\beta 0.1$ -H4, which starts with $H_\beta = 4$ and $\beta \approx 0.01$, so that it loses significant flux before reaching a state similar to $\beta\text{R}0.1$ (cf. Fig. 8); the middle panel shows $\beta 0.05$, which has less flux to lose over its initial phase, but behaves analogously, settling into a similar state (other than its smaller H_{th}) once $\beta \simeq 1$ in the midplane. The lower panel shows $\beta 0.01$ -hr, which is refined from the steady state of $\beta 0.01$ at $t_{\text{refine}} \approx 72\pi/\Omega$ (see text). The refined version decreases in time, resettling into a somewhat higher- β midplane, even though over the same time period the coarser-resolution version $\beta 0.01$ increases its midplane field somewhat (the black lines show $\beta 0.01$ at the same time as the yellow lines for $\beta 0.01$ -hr). This illustrates that the lower- β midplanes seen in $\beta 0.01$ and $\beta 0.001$ (and other cases not shown) are likely the result of poor resolution of H_{th} .

§4.2). Below (§6), we will argue that the field is being continuously regenerated over this phase in a similar way to the true saturated state, but that this regeneration is slower than its expulsion through the boundaries.

Two ZNVF simulations in table 1 stand out as exceptions to the above scenario: $\beta 0.01$ and $\beta 0.001$, which both saturate with a $\beta \ll 1$ midplane (see Fig. 4b; for $\beta 0.001$ especially the gas is everywhere magnetically supported, with no P_B dip at $z = 0$). The thermal scale heights of these simulations are poorly resolved, with only $\simeq 9$ zones in the thermal midplane ($|z| < H_{\text{th}}$) for $\beta 0.01$, and only $\simeq 3$ zones for $\beta 0.001$. A natural hypothesis is thus that the resolution halts the collapse of ρ to the thermal scale height thereby artificially halting the collapse at $\beta \ll 1$. We test this in the lower panel of

Fig. 10 by taking a snapshot of $\beta 0.01$ in the saturated state ($t_{\text{refine}} = 72\pi/\Omega$) and refining its resolution by a factor of two.⁸ We compare the evolution of this refined simulation ($\beta 0.01$ -hr) to the unrefined version over the same time period. While P_B actually increases modestly over this period for $\beta 0.01$ (cf. purple and black lines), that of $\beta 0.01$ -hr decreases (cf. purple and yellow lines). Although it saturates again with $\beta < 1$ in $\beta 0.01$ -hr, this does support the general idea that $\beta \ll 1$ midplanes are likely a result of insufficient resolution, at least in the shearing box and without net vertical flux. Nonetheless, it is interesting — and perhaps physically important despite its unphysical origin — that halting the collapse of the density in the midplane also halts the loss of flux through the boundaries at $z \gg H_{\text{th}}$. We will return to this point in the discussion (§7).

We probe the approach to the saturated state more generally in Fig. 11, which plots the density scale height, $H_\rho \equiv \int dz |z| \rho / \int dz \rho$, and β averaged over $|z| \leq H_\rho$ (termed β_{mid} ; note this is slightly different to β_{mid} in Fig. 5, which averages over $|z| \leq H_{\text{th}}$). The relationship between H_ρ and β_{mid} is effectively probing the equilibrium — lower β generally causes a wider density profile unless P_B becomes flat — so the scatter plot of a simulation’s evolution in β_{mid} - H_ρ space provides a crude measure of how flux is lost over the quasi-equilibrium phase (small markers) and where it settles at saturation (large markers). We see that all simulations collapse onto one path, as expected, starting at lower β (higher H_ρ) then moving to the right and down as they lose flux (the spacing of the points indicates the rate of decrease⁹). $\beta 0.001$ and $\beta 0.01$ stop at lower β , as described above, as do cases with net vertical flux. The final β_{mid} of the other cases seems to increase modestly with coarser resolution (e.g., compare $\beta 0.1$ -mr or $\beta 0.1$ -LorH with $\beta R0.1$; see also App. B) and decrease modestly with L_z/H_{th} (e.g., compare $\beta 0.05$ or $\beta 0.01$ -hr with various $\beta 0.1$ cases). However, there also appears some randomness involved in the details of the final state (indeed, it also changes slowly in time); longer-time, finer resolution simulations are needed to better probe this collapse when $H_{\text{th}} \ll L_z$ and $\beta \ll 1$. In this context, static mesh refinement would be valuable in order to resolve small midplane scales ($\ll H_{\text{th}}$), while avoiding the extremely costly timestep limitations that result from the strongly magnetized upper layers.

6. SUSTAINING THE LOW- β STATE

In this section we study how the low- β state is maintained via a dynamo feedback that regenerates flux lost through the boundaries. We do not consider the high- β cycles, since this has been studied extensively in past work (e.g., Lesur & Ogilvie 2008b; Squire & Bhattacharjee 2015a; Gressel & Pessah 2015), focusing instead on how the system can maintain strong time-independent mean fields. (Note that the term “dynamo” is sometimes used to refer specifically to cyclic behavior in the

⁸ At t_{refine} the shear-periodic boundary conditions are truly periodic, allowing straightforward refinement over the x boundaries.

⁹ $\beta 0.01$ exhibits a very long phase of more slowly increasing β (see also Fig. 5), which apparently occurs once the collapse of ρ is strongly affected by resolution, but not yet completely halted.

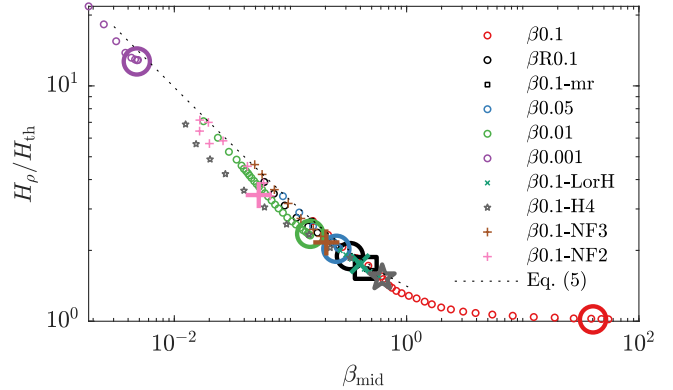


FIG. 11.— The relation between the density scale height, H_ρ and β averaged over $|z| \leq H_\rho$ (β_{mid}), for a number of simulations from table 1. Small markers illustrate time slices separated by approximately 1 orbit ($t\Omega = 6$), while the large markers indicate an average over the steady state. The dashed line shows the same quantities computed from the equilibrium (5), which is effectively $H_\rho \propto \beta^{-1/2}$ at $\beta \ll 1$.

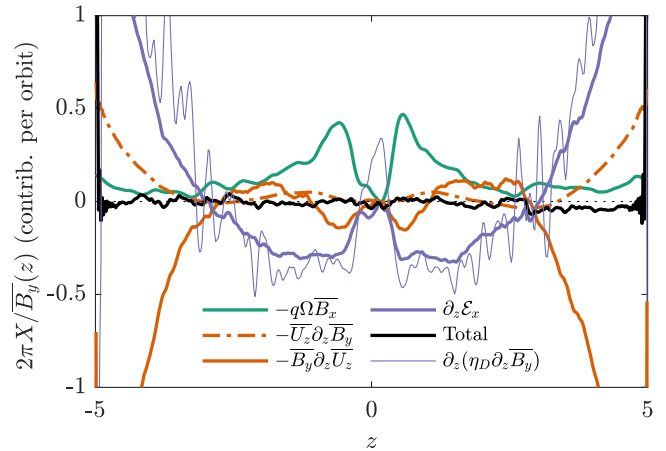


FIG. 12.— Terms in the equation for $\partial_t \overline{B}_y$ in $\beta R0.1$, averaged over the steady state in time (see Eq. (10)). We see that near the midplane, B_y flux is supplied by the shearing of \overline{B}_x , which is balanced by transport to higher $|z|$ from the turbulence ($\partial_z \mathcal{E}_x$) with small contributions from mean outflows on either side of the midplane. In contrast, at large $|z|$, \overline{B}_y is sustained primarily by the upwards transport of flux by the turbulence ($\partial_z \mathcal{E}_x$), which competes against strong vertical outflows through the boundary. This shows that, absent a dynamo effect to regenerate \overline{B}_x , the field would decay within several orbits. The thin purple line compares the measured $\partial_z \mathcal{E}_x$ with the dynamo-theory result $\mathcal{E}_x \approx \eta_{\text{turb}} \partial_z B_y$ with $\eta_{\text{turb}} = \Omega^{-1} \overline{\delta \mathbf{u}^2} / 3$ (we smooth this with a 5-gridpoint moving average for clarity).

accretion-disk literature, but here we use it more generally to describe the mechanism by which a large-scale field is generated.) While we provide clear evidence that fields are regenerated and expelled on several-orbit time-scales — viz., the system does not reach steady state because its activity shuts down, but because flux loss and growth are balanced — the physics of this mechanism, and how this depends on parameters, remain poorly understood.

6.1. Mean-field dynamo: background

An x, y average of the radial and azimuthal components of the induction equation (1c) yields

$$\partial_t \overline{B}_x = -\partial_z(\overline{U}_z \overline{B}_x) + \overline{B}_z \partial_z \overline{U}_x - \partial_z \mathcal{E}_y, \quad (10a)$$

$$\partial_t \overline{B}_y = -q\Omega \overline{B}_x - \partial_z(\overline{U}_z \overline{B}_y) + \overline{B}_z \partial_z \overline{U}_y + \partial_z \mathcal{E}_x, \quad (10b)$$

where $\mathcal{E} \equiv \overline{\delta \mathbf{u}} \times \overline{\delta \mathbf{B}}$ is the turbulent electromotive force (EMF) from the fluctuations. In Eq. (10b), the first term captures the stretching of the radial field to azimuthal by the mean shear flow, the second captures advection and compression/rarefaction by the vertical outflow, the third captures stretching of a vertical field in a z -dependent shear (note that $\nabla \cdot \mathbf{B} = 0$ implies $\overline{B}_z = 0$ unless there is a net vertical flux), and the fourth term captures the effect of the fluctuations on the mean field. In the traditional mean-field dynamo paradigm (Brandenburg & Subramanian 2005; Rincon 2019), \mathcal{E} is Taylor expanded assuming the fluctuations are small scale compared to the mean, yielding

$$\begin{aligned} \mathcal{E}_i &\approx \alpha_{D,ij} \overline{B}_j + \tilde{\eta}_{D,ijk} \partial_j B_k + \dots \\ &\sim \alpha_D \overline{B}_i - \eta_D (\nabla \times \overline{\mathbf{B}})_i, \end{aligned} \quad (11)$$

where the ‘transport coefficients’ α_D and η_D are determined by the dependence of the fluctuations on the mean fields. The second expression results from assuming homogeneous and isotropic fluctuations, which, while not valid in a stratified shear flow, is helpful for the simple analysis carried out here (α_D is the diagonal part of $\alpha_{D,ij}$; η_D is the fully antisymmetric part of $\tilde{\eta}_{ijk}$). The so-called α - Ω dynamo results for non-zero α_D , when the strong \overline{B}_y generates \overline{B}_x via the final term in Eq. (10a), which then regenerates \overline{B}_y via $-q\Omega \overline{B}_x$. The effect can be understood as a linear instability by ignoring the effect of \overline{U}_z and inserting Eq. (11) into (10), then assuming $\overline{B}_i \propto e^{i\kappa z}$ and $|\alpha_D \kappa| \ll q\Omega$; one finds solutions with frequency $\omega_D \approx -i\kappa^2 \eta_D \pm \sqrt{i\kappa \alpha_D q\Omega}$, such that a branch of growing and oscillating solutions exists at small κ , where the dynamo feedback (via α_D) overcomes the turbulent diffusion (via η_D). The crux, of course, is having fluctuations that cause a sufficiently large α_D , which can result from the combination of stratification and rotation creating a net helicity $\overline{\delta \mathbf{u}} \cdot \nabla \times \overline{\delta \mathbf{u}}$ or current helicity $\overline{\delta \mathbf{B}} \cdot \nabla \times \overline{\delta \mathbf{B}}$. This formalism, or extensions of it, has been analysed in a number of papers in order to understand the cyclic behavior of the high- β state (see, e.g., Gressel & Pessah 2015; Mondal & Bhat 2023 and references therein). It is also possible to have a similar large-scale dynamo with $\alpha_D = 0$ as a result of off-diagonal components of $\tilde{\eta}_{D,ijk}$ (Rädler & Stepanov 2006; Squire & Bhattacharjee 2015b; Mondal & Bhat 2023).

6.2. Sustaining a strong azimuthal field against escape

Mean-field theory is applied to the saturated low- β state in Fig. 12. We illustrate the time average over the steady state of each term in Eq. (10b), normalizing each by $\overline{B}_y(z)/2\pi$, such that a value of 1 implies that the particular term would grow or decay \overline{B}_y by a factor $e^{\pm 1}$ over one orbit at each z . The sum over all terms is effectively zero, as must be the case in steady state.

Our general conclusions are similar to Johansen & Levin (2008) (figures 11-14), with the important difference that flux is continuously escaping the bound-

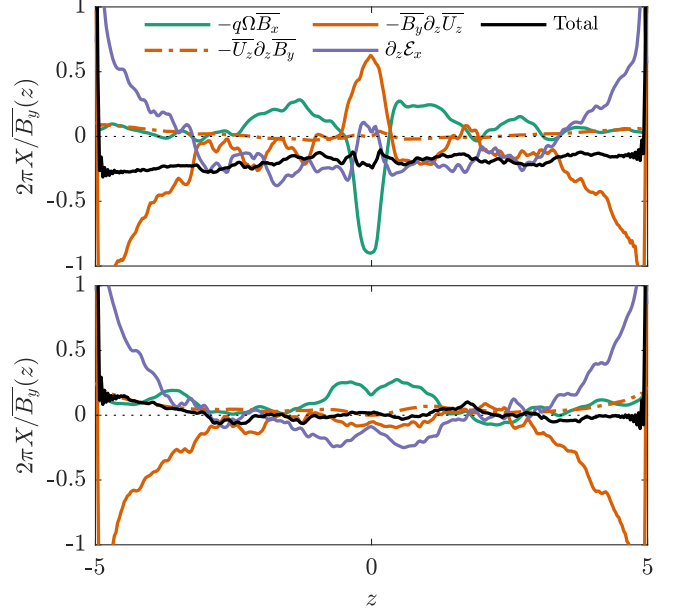


FIG. 13.— As in Fig. 12, but for the cases $\beta 0.1$ -H4 (top) during its collapse phase (averaged from $t\Omega/2\pi \approx 6$ to 8; cf. Fig. 10) and $\beta 0.001$ (bottom).

aries in our case. Fields are replenished and expelled over several-orbit timescales, with strong flux creation by shearing for $H_{\text{th}} \lesssim |z| \lesssim 3$ balanced by its diffusion to larger $|z|$ by turbulence ($\partial_z \mathcal{E}_x$). For $|z| \gtrsim 3$, \overline{B}_y is instead replenished by fluctuation-induced diffusion from smaller z (i.e., turbulent transport; $\partial_z \mathcal{E}_x$), while being rapidly carried out of the box by the expanding outflows ($\overline{B}_y \partial_z \overline{U}_z$; advection by \overline{U}_z is only a minor effect because \overline{U}_z is purely compressive). With the thin purple line, we compare the measured $\partial_z \mathcal{E}_x$ from $\overline{\delta \mathbf{u}} \times \overline{\delta \mathbf{B}}$ to the expected η_D from quasi-linear dynamo theory, $\eta_D = \overline{\delta \mathbf{u}^2}/3\Omega$, assuming the correlation time of the turbulence is $\simeq \Omega^{-1}$ (there is no contribution to η_D from $\overline{\delta \mathbf{B}}$ fluctuations in quasi-linear theory; Rincon 2019). We see surprisingly good agreement, with $\partial_z \mathcal{E}_x \approx \partial_z (\eta_D \partial_z \overline{B}_y)$ across the full domain; this indicates that the fluctuations are predominantly affecting \overline{B}_y as a turbulent diffusion, as expected (the effect of a possible α_D on $\partial_t \overline{B}_y$ would be very small, being proportional to \overline{B}_x).

Figure 13 shows the same \overline{B}_y -dynamo analysis for two other cases of relevance. The first, $\beta 0.1$ -H4, is discussed in §5.5; it starts from $\beta \ll 1$ and loses all of its flux until reaching $\beta \sim 1$ in the midplane. We consider the middle of this flux-decrease phase, averaging from $t\Omega/2\pi \approx 6$ to 8 (fourth to sixth line from the top in Fig. 10a), but the results are similar at all times during this phase. As expected, the total \overline{B}_y contribution from all terms is nearly constant and negative, indicating \overline{B}_y is decreasing in time without changing shape. But, we also still see robust field creation for $|z| \gtrsim H_{\text{th}}$, and the balance of terms is similar to the true saturated state in Fig. 12. In other words, during this flux-decrease phase, a similar dynamo continues to operate, but the growth via $q\Omega \overline{B}_x$ is overwhelmed by the turbulent diffusion and outflows. The properties for $|z| \lesssim H_{\text{th}}$ are explained by our previous observations that the midplane density is increasing by inwards collapse (thereby requiring a large positive contribution from \overline{U}_z) but the midplane \overline{B}_y is not (thereby

requiring a large negative contribution from $\overline{B_x}$ to balance that from $\overline{U_z}$. How the system conspires to reverse the midplane $\overline{B_x}$ in order to achieve this is not at all obvious, but it is nonetheless effectively guaranteed if $\overline{B_y}(z, t)$ is to maintain a similar spatial form as the total flux decreases.

The second example in Fig. 13 is $\beta 0.001$, which maintains a $\beta \ll 1$ midplane because the collapse of density is halted by the simulation's low number of grid cells per H_{th} . While it is not surprising that the coarse grid stops the density's collapse to $\simeq H_{\text{th}}$, the observation that this *also* stops the escape of flux is interesting (see also §5.5). Indeed, we see that the system's dynamo continues to operate, supporting the field against the turbulent diffusion in the midplane and rapid outflows to the boundaries. While the loss/growth rate is somewhat lower than in the resolved case ($\beta R0.1$; Fig. 12), it still implies complete regeneration of the flux over 4 to 5 orbits in regions away from the midplane that should, in principle, be ignorant of H_{th} and thus adequately resolved. Note also that the near-midplane turbulence in this simulation is highly supersonic, as needed to cause a similar relative $\partial_z \mathcal{E}_x$ at $\beta \ll 1$.

A simple interpretation of these results is that, in principle, any $\beta \ll 1$ state can be maintained, with the dynamo generating a $\overline{B_x}$ near the midplane that in turn balances the continual loss of $\overline{B_y}$ through the boundaries. However, without a reason for the density to stop at a particular scale height H_ρ , it always collapses towards a thermal profile in the midplane, with the magnetic field (and thus the dynamo) being forced to cooperate. It stops once P_{th} provides significant pressure support, corresponding to the $\beta \sim 1$ midplane in the steady state of well-resolved simulations. On the other hand, if other effects intervene — the grid in our simulations, but perhaps e.g., radiation, or physical midplane turbulence from another source in more realistic settings — the collapse is halted with $H_\rho \gg H_{\text{th}}$, thereby also enabling a $\beta \ll 1$ midplane.

6.3. Generation of the radial field

The results of Eq. (10b) and Fig. 13 show only that $\overline{B_y}$ is driven primarily by $\overline{B_x}$, providing no information on $\partial_t \overline{B_x}$, which must also be continuously regenerated to balance its escape. Unfortunately a similar analysis for $\overline{B_x}$ is less useful: $-\partial_z \mathcal{E}_y$ can provide both turbulent diffusion through η_D , and growth of $\overline{B_x}$ through $\mathcal{E}_y \sim \alpha_D \overline{B_y}$; absent other contributions from mean flows, the two effects will generally cancel so that $\partial_t \overline{B_x} \approx 0$. This implies that $\partial_z \mathcal{E}_y \approx 0$ does not yield useful information about the relative sizes of growth and diffusion terms. While a number of techniques have been developed to overcome this and measure α_D and η_D in simulations (e.g., the “test-field” method; Schirmer et al. 2005), all have limitations and are rather complex, falling beyond the scope of this paper. Instead, motivated by the apparent success of quasi-linear dynamo theory for predicting $\partial_z \mathcal{E}_x$ (thin purple line in Fig. 12), here we attempt to test the basic α - Ω dynamo paradigm in which α_D is driven by the fluctuations' helicity, using the simplest, standard quasi-linear result for helical velocity and magnetic fluctuations:

$$\alpha_D \approx -\frac{1}{3\Omega} (\overline{\delta \mathbf{u} \cdot \nabla \times \delta \mathbf{u}} - \overline{\delta \mathbf{B} \cdot \nabla \times \delta \mathbf{B}} / \rho). \quad (12)$$

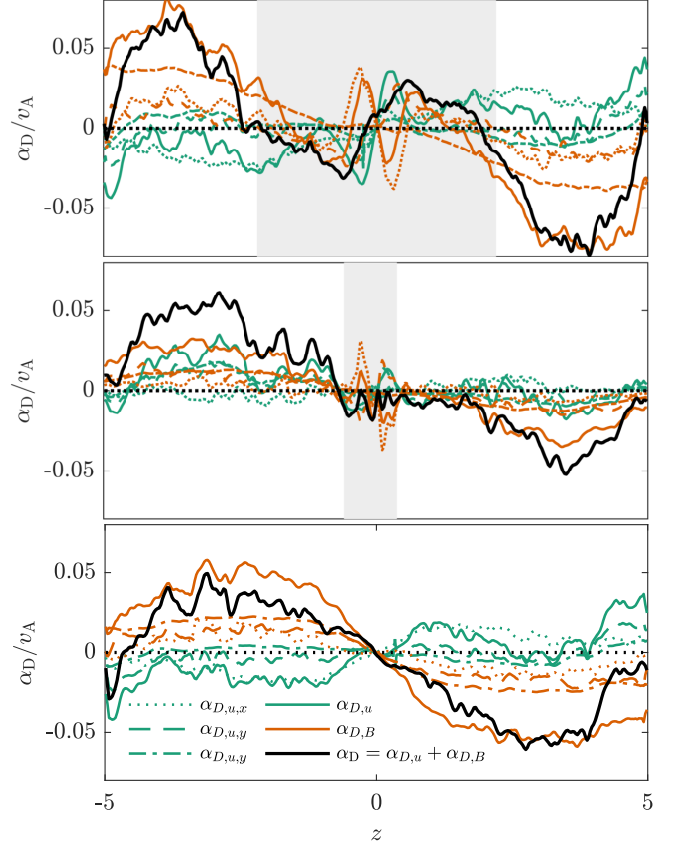


FIG. 14.— Estimate of α_D from mean-field dynamo theory based on the helicity of the fluctuations (Eq. (12)). We show the three simulations from Figs. 12 and 13 ($\beta R0.1$, $\beta 0.1$ -H4 from $t\Omega/2\pi = 4$ to 6, and $\beta 0.001$ from top to bottom). The shaded regions show where $\beta > 0.03$, which seems empirically to predict the sign of α_D . Although α_D is sufficiently large to explain the mean-field dynamo for the parameters we consider, it does not exhibit the required sign in $\beta > 0.03$ regions, and moreover, this sign changes between cases that otherwise seem to exhibit similar dynamo mechanisms.

We again assume a correlation time Ω^{-1} (Pouquet et al. 1976; Rincon 2019). This α effect then enters the mean induction equation (10a) as $-\partial_z(\alpha_D \overline{B_y})$, so this form of dynamo feedback would require $\alpha_D \leq 0$ at $z > 0$ since $\overline{B_x} < 0$ is needed to drive $\overline{B_y} > 0$ when $\partial_z \overline{B_y} < 0$ (likewise, $\alpha_D > 0$ at $z < 0$).¹⁰ To estimate the value of α_D that would be required to drive the observed dynamo, we can use the approximate power-law equilibrium (4) with $v_A/\Omega = z\sqrt{2/a}$ to write $\partial_z \mathcal{E}_y \sim \alpha_D \partial_z \overline{B_y} \sim \sqrt{a/2\Omega} \overline{B_y} \alpha_D / v_A$ (where $a/2 = |\partial \ln \overline{B_y} / \partial \ln z|$). Thus, to regenerate $\overline{B_x}$ in one orbit requires $\alpha_D / v_A \simeq (2\pi)^{-1} \sqrt{2/a} \overline{B_x} / \overline{B_y}$; we have $|\overline{B_x} / \overline{B_y}| \lesssim 0.05$ in ZNVF flux cases, suggesting $\alpha_D / v_A \sim 0.01$ should be sufficient to sustain the dynamo.

We test these ideas in Fig. 14 for the simulations shown in Figs. 12 and 13, all of which exhibit a continuously regenerated $\overline{B_x}$. As well as Eq. (12), we plot the contribution from each direction of $\delta \mathbf{u}$ and $\delta \mathbf{B}$ fluctuations ($\alpha_{D,u,x} = -\delta u_x (\nabla \times \mathbf{u})_x / 3\Omega$, $\alpha_{D,B,y} =$

¹⁰ In principle, the expression $-\partial_z(\alpha_D \overline{B_y})$ could allow a dynamo driven by an α_D gradient instead, in which case $\partial_z \alpha_D > 0$ would be needed. However, this is not the standard α - Ω mechanism and many other terms beyond the simple scalar expansion for α_D in Eq. (11) may become important also.

$\overline{\delta B_y}(\nabla \times \mathbf{B})_y/3\Omega$ etc.) to attempt to extract general features and trends. Most importantly, although the magnitude of α_D is in principle sufficiently large to produce the observed dynamo feedback, we see no consistent sign of α_D between each of the 3 cases shown, including for $\alpha_{D,u}$ and $\alpha_{D,B}$ individually (this could be relevant, for example, if the magnetic contribution to α_D in Eq. (12) was more or less efficient at driving a dynamo than the velocity contribution; see e.g., Gressel 2010; Rincon 2019). Instead, we find empirically that the sign of α_D seems to be well predicted by whether $\beta > 0.03$ (grey-shaded regions; $\alpha_D > 0$), or $\beta < 0.03$ ($\alpha_D < 0$), a feature that seems robust across all of our simulations, including those with net vertical flux (not shown). This change is driven primarily by the stronger magnetic fluctuations at low β , and may relate to a greater dominance of the Parker instability compared to the MRI, although this is hard to diagnose. $\beta R_0.1$ is of particular relevance to our overall conclusion: with $\alpha_D > 0$ at $z > 0$, it would not sustain the observed $\overline{B_x}$ if Eq. (12) were correct, despite apparently having a rather similar dynamo to $\beta 0.1\text{-H4}$ and $\beta 0.001$ (for which $\alpha_D < 0$ at $z > 0$).

We thus conclude that the dynamo mechanism regenerating $\overline{B_x}$ is likely not the standard α effect driven by flow or current helicity. This is consistent with previous simulations of buoyancy-driven large-scale dynamos, which have seen similar inconsistencies between the measured sign of helicity and theoretical expectations (e.g., Tharakal et al. 2023, and references therein). One possible explanation is that there exist two mechanisms — driven, e.g., by MRI or the Parker instability — which can both provide the required dynamo feedback but in different ways (e.g., in low- β Parker-dominated regions, α_D does have the required sign). This resembles ideas proposed in Johansen & Levin (2008) and is also consistent with analyses of differences between midplane and coronal regions in the high- β state (Gressel 2010; Held et al. 2024). Similarly, the analysis of Held et al. (2024) suggests that local vertical fields play a key role in low- β regions, generating radial fields via vertical gradients in the flow; this interplay would not show up in our analysis to our horizontal average but would be interesting to study further in the low- β state. Another non-exclusive possibility is that the feedback is unrelated to the helicity, instead relying only on the shear flow via off-diagonal $\tilde{\eta}_{D,ijk}$ terms (Rädler & Stepanov 2006; Rogachevskii & Kleeorin 2008; Squire & Bhattacharjee 2016). This would more easily explain the apparent robustness of the field regeneration, but, other than at low Reynolds numbers (Squire & Bhattacharjee 2015c), the properties of this type of dynamo remain poorly understood (Käpylä et al. 2020; Zhou & Blackman 2021; Mondal & Bhat 2023).

6.4. The dynamo loop with net vertical flux

The dynamo mechanism with net vertical flux requires separate attention, both because of previous results and because it operates differently. In Fig. 15 we plot (for $\beta_z = 100$), the dynamo contributions from Eq. (10) for both $\overline{B_y}$ (as in Fig. 12) and $\overline{B_x}$, each normalized as before to show the relative contribution per orbit at each z . The $\overline{B_y}$ balance shows significantly stronger outflows than in Fig. 12, balanced by a larger shear-generation term, $-q\Omega\overline{B_x}$ due to its strong $\overline{B_x}$ (this also causes the large mean magnetic field $\alpha_{\overline{B}} \approx \alpha$ contribution in

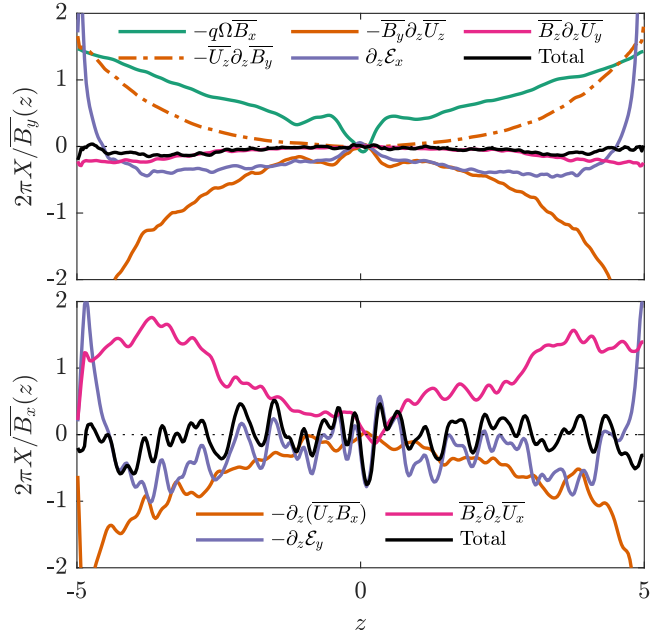


FIG. 15.— Dynamo contributions for $\beta 0.1\text{-NVF2}$ with net vertical flux. The top panel shows the same analysis as Fig. 12, again showing that $\overline{B_y}$ is regenerated against very strong outflows by stretching of the radial field ($-q\Omega\overline{B_x}$), though with a rather different form to the ZNVF case and $\partial_z \mathcal{E}_x < 0$ across effectively the full domain. The lower panel shows the same analysis for $\overline{B_x}$, with terms normalized to $\overline{B_x}/2\pi$ such that they again represent the relative contribution per orbit. We see that $\overline{B_x}$ is sustained by a self-generated vertical shear of $\overline{U_x}$ stretching the (constant) mean B_z ($\overline{B_z}\partial_z\overline{U_x}$). This shows that the NVF case is sustained by a laminar dynamo; effectively a single large-scale MRI channel mode (see text).

Fig. 9e). Fluctuations, which have a similar amplitude to the ZNVF low- β states, play little role in the balance (see Fig. 9d). In the lower panel, we see that $\overline{B_x}$ is also being sourced in a laminar way, via stretching of the mean $\beta_z = 100$ vertical field by a self-induced vertically sheared radial flow ($\overline{B_z}\partial_z\overline{U_x}$).

This behavior, which is clearly different from that at ZNVF, is simply the manifestation of a single, box-scale MRI channel mode developing across the domain. Indeed the relative signs, symmetries, and sizes of \overline{B} and \overline{U} in this $\beta_z = 100$ state are similar to those of a growing MRI mode. The solution resembles that discussed in the context of winds in Lesur et al. (2013) but with the opposite symmetry: here and in Bai & Stone (2013), $\overline{B_y}$ has a peak in the midplane (like $\cos(z)$); for the solutions in Lesur et al. (2013), $\overline{B_y}$ passes through zero at $z = 0$ (like $\sin(z)$). By extension, effectively all of the angular momentum stress comes from this channel mode, explaining the strong dominance of $\alpha_{\overline{B}}$ compared to the turbulent contributions.

An additional important feature is that the symmetry of this $\overline{U_x}$ may not be possible to realize in global simulations. In particular, as pointed out by Bai & Stone (2013) in the context of the outflow/wind (see their figure 12), this $\partial_z\overline{U_x} > 0$ requires that $\overline{U_x}$ and $\overline{B_x}/\overline{B_z}$ have opposite signs above and below the midplane, implying a radial inflow for $z > 0$ and outflow for $z < 0$ or vice versa (depending on the sign of B_z). The flow is also fast ($\overline{U_x} \gtrsim c_s$ at larger z ; Bai & Stone 2013) thereby

requiring a strongly asymmetrical corona that seems at odds with those expected and observed in corresponding global simulations. Indeed, rather than the single-signed strong toroidal field seen here and in past local studies, [Zhu & Stone \(2018\)](#); [Mishra et al. \(2020\)](#) observe a sign flip in \overline{B}_y (and \overline{B}_x) across the midplane, with approximately symmetric inflow both above and below the midplane. We note that this state still appears to have the structure of a single large-scale channel mode, albeit one with the same symmetry as those studied by [Lesur et al. \(2013\)](#). This change causes $\beta \gtrsim 1$ in the midplane of the global solution of [Mishra et al. \(2020\)](#) at $\beta_z = 100$, although the accretion stress above and below remains mean-field dominated. While further study of these solutions is clearly needed, the analysis helps to elucidate the cause of the strong influence of net flux on both local and global simulations — it destabilizes a box-scale MRI mode, which then dominates the generation of the mean fields and angular momentum transport, driving strong outflows.

7. DISCUSSION & CONCLUSIONS

In this work, we have introduced and characterized a novel strongly magnetized state of self-sustaining accretion disk turbulence in the local stratified shearing box. The system maintains a strong mean azimuthal field in the midplane, with $\beta \lesssim 1$, modestly sub-Alfvénic fluctuations ($|\delta\mathbf{B}| \lesssim \overline{B}_y$), and large accretion stresses, $\alpha \simeq 0.5$. A net vertical flux — traditionally thought to be necessary to sustain such large α — is not required, although the field structure and turbulence properties do superficially resemble previous NVF results (e.g., [Bai & Stone 2013](#)) even though the sustenance mechanism of the ZNVF state is different. So long as the vertical domain size is sufficiently large (in units of H_{th}), the state is also robust to choices of vertical boundary conditions and numerical options — indeed, we show explicitly that the azimuthal flux is continuously escaping through the boundaries.

We argue that the transition to this low- β state, as opposed to the well-known high- β cyclic dynamo discussed in many previous works (e.g., [Davis et al. 2010](#); [Simon et al. 2012](#)), is controlled by the initial magnetization of the midplane: if there is sufficient azimuthal flux after the initial conditions rearrange to create a $\beta \lesssim 1$ midplane and $\beta \ll 1$ corona, the system can maintain the low- β state; if there is not, it inevitably loses all midplane flux, transitioning into high- β dynamo cycles. The initial azimuthal (or radial) flux thus acts like a “switch” between two states of vastly different α in a system with otherwise identical parameters. Empirically we find that an initial $\beta \simeq 0.1$ in the initial Gaussian toroidal field is the dividing line between the disk evolving to the low- β or high- β state. Given the well-known convergence and microphysics dependence of ZNVF shearing box results in the high- β state ([Fromang et al. 2007](#); [Ryan et al. 2017](#)), the transition between the two states found here, and indeed the properties and existence of the low- β state, may also be sensitive to these physical and numerical parameters. This should clearly be studied more in future work, where mesh refinement may be helpful in allowing the thermal midplane to be better resolved than has been possible here. The importance of turbulent magnetic flux transport in determining the proper-

ties of the low- β state also specifically motivates future simulations with explicit resistivity and varying magnetic Prandtl number.

Given the variety of rapid state transitions observed in X-ray transients, dwarf novae (e.g. [Smak 1984](#)) and changing-look AGN ([Ricci & Trakhtenbrot 2023](#)), the strong dependence of the efficiency of angular momentum transport on the “initial” magnetic field may be of particular interest. For instance, in dwarf novae, α is seen to vary in between $\alpha \sim 0.1$ - 0.4 in the hot state and $\alpha \sim 0.01$ - 0.03 in the cold state ([King et al. 2007](#); [Kotko & Lasota 2012](#)), rather similar to the difference seen here between the low- and high- β states, while X-ray binaries may exhibit yet higher $\alpha \sim 0.2$ - 1 ([Tetarenko et al. 2018](#)). While changes in the net vertical flux, the MRI, and/or winds can potentially explain this variability (e.g., [Gammie & Menou 1998](#); [Hirose et al. 2014](#); [Begelman & Armitage 2014](#); [Scepi et al. 2018](#); [Zhu & Stone 2018](#)), as well as mechanisms unrelated to changes in the magnetic field (e.g., [King & Ritter 1998](#); [Scepi et al. 2024](#)), the possibility hinted at by our results has the nice feature that extra magnetic flux in *almost any configuration* (toroidal, radial, or vertical) could be sufficient to cause significant changes in the efficiency of angular momentum transport. For instance, in feeding such a disk, if a parcel of gas with higher-than average magnetic field caused the toroidal field strength to cross the $\beta \lesssim 1$ threshold, it would trigger the transition from the high- to low- β state. As seen in [Machida et al. \(2006\)](#), whose global simulations reach a $\beta \sim 0.1$ state with similar properties to that studied here, the same could occur if the disk undergoes a thermal collapse, amplifying the toroidal field by flux freezing. This would result in significantly more rapid accretion, potentially then depleting the disk of magnetic flux and density to cause an eventual transition back to the high- β state. This scenario is not necessarily at odds with various previous proposals; the new insight here is that the magnetic-field strength adds bimodality to the local turbulence, with large, sudden changes to α resulting from small changes in disk parameters. However, further study with more a detailed treatment of radiation is certainly needed, for instance to understand whether such transitions, which occur over tens of orbital periods in our simulations, disagree with observed smoother transitions through intermediate states (e.g., [Skipper & McHardy 2016](#)).

7.1. The cause of the state transition

In the course of analysing the low- β state and its transition to the high- β state, we have run a wide variety of simulations with different initial conditions and other options, leading to various more detailed conclusions. These are listed in §2, to which we refer the reader for a more in depth summary of our computational results. Forgoing a summary here, we instead propose a scenario for how the system attains bimodality, giving rise to the distinct low- and high- β states. This physics remains far from certain — indeed our attempts at diagnosing the field-generation mechanism remained partially unsuccessful (see §6.3) — but may provide a helpful framework for further development. The scenario has three main elements:

(1) *Azimuthal flux must be continuously generated*— The disk midplane and its atmosphere are highly unstable,

exhibiting strong trans- and super-sonic turbulence. This rapidly transports flux upwards, implying that in order to sustain itself, the system must continuously generate flux through a (non-cyclic) large-scale dynamo. The flux is regenerated and removed on several-orbit timescales, as shown in Figs. 12 and 13, implying the dynamo must be efficient and robust. Given that the mean shear generates strong azimuthal flux from radial flux, the turbulent fluctuations must generate radial flux from azimuthal flux to “close the loop.”

(2) *Parker-instability-driven turbulence generates radial from azimuthal flux*— Both the Parker instability and MRI seem to play important roles in maintaining the low- β state, as evidenced by the similarity of the midplane turbulence to the high- β state (Fig. 6), our simple turbulence model (Fig. 7), and previous works (Johansen & Levin 2008; Held et al. 2024). However, evidence suggests that fluctuations driven by the Parker instability generically and naturally generate azimuthal from radial flux, with MRI playing a subsidiary role. First, even when the system is not in steady state with β increasing in time, the dynamo still operates (flux is just being lost faster than it is created; Fig. 13); in this regime $\beta \ll 1$ so the MRI is suppressed (likewise $\beta \ll 1$ resolution-limited states sustain a dynamo). Second, in the midplane ($|z| \lesssim H_{\text{th}}$) the net radial field is absent or of the wrong sign to support the dynamo (Figs. 2 and 12); this is presumably where MRI drives turbulence, since the Parker instability is stable. Together these suggest that Parker-driven fluctuations drive the dynamo itself, while MRI is likely needed to drive midplane turbulence that can diffuse \overline{B}_y to maintain the strongly magnetized midplane.

(3) *As β grows, the Parker instability shuts off near the midplane*— This is a simple consequence of the Parker instability criterion, $z \partial \ln B_y / \partial z < 0$ (see §4.2), and the magnetized equilibrium. For $\beta_{\text{mid}} \gtrsim 1$, gravitational support is provided by thermal rather than magnetic pressure, implying that P_B flattens (or reverses its gradient) some distance above the midplane. Thus, as β_{mid} rises above unity, the Parker-unstable region moves further from the midplane to larger $|z|/H_{\text{th}}$.

Together with points (1) and (2) — that the Parker instability is needed for sustaining the azimuthal flux, which rapidly escapes if it is not continuously regenerated — point (3) implies that the Parker-induced feedback becomes less efficient at regenerating the mean field for $\beta_{\text{mid}} \gtrsim 1$. This would then further raise β by its inability to regenerate more flux, running away until the flux is completely expelled from the midplane. Thus results the high- β state, which presumably sustains turbulence via a different midplane mechanism (unrelated to the Parker instability) exhibiting characteristic ~ 10 -orbit reversal of $\overline{\mathbf{B}}$, $\delta \mathbf{B} \gg \overline{\mathbf{B}}$, and $P_B \ll P_{\text{th}}$. This scenario thus qualitatively explains why the system switches states based on the initial flux, with no “intermediate” state available (see Fig. 5) — as β_{mid} rises above unity, the feedback mechanism becomes continuously weaker. If we further assume that the primary role of the MRI is to generate midplane turbulence, the scenario remains consistent with the behavior at $\beta \ll 1$. Specifically: (i) a steady state with $\beta \ll 1$ cannot be maintained despite a similar dynamo, because the MRI fails to sustain supersonic

turbulence at $z = 0$ (where Parker instability shuts off), which would be required to support a density scale height $\gg H_{\text{th}}$; and (ii) in contrast, a steady state with $\beta \ll 1$ can persist if resolution is insufficient — when the midplane is poorly resolved, physical (turbulent) diffusion is replaced by numerical diffusion, preventing the collapse of the density.

7.2. Subsidiary results

In addition to the main results of this work, we have noted subsidiary results relating to the high- β dynamo cycles and turbulence with net vertical flux:

Dynamo cycles— Periodic reversals of \overline{B}_y , which have been traditionally associated with the MRI, appear to persist in the absence of rotation, albeit with some morphological differences (see App. D, Fig. 19). This does not seem to disagree with previous works, which mostly have not explored the effect of setting $\Omega = 0$, but may be of interest for understanding the mechanism via which this turbulence self sustains (idealized dynamo-focused simulations exhibit cyclic behavior without rotation, so this is perhaps not unexpected; e.g., Brandenburg et al. 2008; Squire & Bhattacharjee 2015b). Similar cycles are also observed with a net vertical flux in the absence of rotation (Fig. 20).

MRI channel modes with net vertical flux— With strong NVF ($\beta_z \lesssim 100$), the large angular momentum transport is almost entirely driven by the mean magnetic-field stress ($\alpha_{\overline{\mathbf{B}}} = -\overline{B}_x \overline{B}_y$; Bai & Stone 2013), with \overline{B}_x and \overline{B}_y maintained by the mean flows ($\partial_z \overline{U}_x$ stretches \overline{B}_z into \overline{B}_x ; the Keplerian flow stretches \overline{B}_x into \overline{B}_y). This structure is effectively a single MRI channel mode stretching across the full vertical extent of the domain, although its appearance is rather similar to the low- β ZNVF state. As also noted by Bai & Stone (2013) in the context of the winds produced by their simulations, the symmetry of the solution likely implies it cannot occur in more realistic, global settings, since it requires strong (supersonic) oppositely directed radial flows on either side of the midplane to sustain the mean fields and large α . Indeed, unlike the shearing box, which exhibits a single-signed \overline{B}_y at any particular time, similar ($\beta_z \approx 100$) global NVF simulations develop strong ($\beta \lesssim 1$) mean fields that reverse their polarity across the midplane (Mishra et al. 2020; see also Zhu & Stone 2018). We note in passing that this global structure in Zhu & Stone (2018); Mishra et al. (2020) is also essentially a single channel mode, but with the opposite symmetry about z : effectively $\overline{B}_y \propto \sin(z)$ and $\overline{U}_x \propto \cos(z)$ in the global domain, rather than $\overline{B}_y \propto \cos(z)$ and $\overline{U}_x \propto -\sin(z)$ in the local one. This change allows the global system to maintain a symmetric flow structure across the midplane.

These aspects, which have only been touched upon in this work insofar as they related to our main results, deserve further study in future work.

7.3. Application to global models and $\beta \ll 1$ fields

Some of the most important questions raised by this work relate to its application to global simulation results, e.g., those of Gaburov et al. (2012), H+24, and Guo et al. (2024). Gaburov et al. (2012) studied the disruption of a magnetized gas cloud by a black hole and found disks with midplane $\beta \sim 0.1$ supported almost entirely

by magnetic pressure. The global multi-physics solutions of H+24, which form self-consistently from cosmological initial conditions via capture of gas from a cloud complex, evolve to an extremely strongly magnetized disk, with β reaching $\sim 10^{-4}$ in the midplane and large accretion rates $\alpha \gg 1$. Guo et al. (2024) studied the fueling of M87* and found that cooling of the hot intra-cluster gas produces a disk dominated by strong toroidal magnetic fields with $\beta \sim 10^{-2}$. Other global simulations have likely also yielded similar states, for instance Machida et al. (2006), who observed a $\beta \sim 0.1$ magnetically supported solution emerge from a cooling disk that contracted vertically, or Sądowski (2016), who reported a thermally stable strongly magnetized disk arising from idealized initial conditions with a net radial field.

Our results capture a number of general features of these solutions, such as the modestly sub-Alfvénic fluctuations and dominant, single-polarity toroidal field. While local simulations with NVF also create strong toroidal fields and some outwardly similar features, the different morphology observed in global simulations with NVF (e.g., Zhu & Stone 2018; Mishra et al. 2020), suggests that the results of H+24, Guo et al. (2024), and Gaburov et al. (2012) do not result from “patches” of vertical field driving the MRI (moreover, these simulations do not appear to involve a vertical field that is at all coherent; see, e.g., H+24 figure 6). The vertical profile shape of the magnetic field and density found here are also very similar to those in H+24 and Guo et al. (2024).

However, one key feature in which our solutions differ markedly is the midplane β : while some of these global disks sustain $\beta \ll 1$ in the midplane, our local simulations always collapse to $\beta \sim 1$ given sufficient resolution. This difference in midplane β is particularly important in understanding AGN, since low β leads to much lower gas densities, which helps the disk avoid fragmentation due to gravitational instability (a long-standing problem in fueling luminous AGN; Goodman 2003).

Given that our local simulations also saturate at $\beta \ll 1$ when H_{th} is poorly resolved (the density collapses to the grid resolution; see Fig. 4), one possible cause of the difference is simply that the global cases are affected by resolution, artificially lowering β . However, it is also plausible that physical processes not captured in the shearing box simulations presented here could play a significant role, leading to differences. Clearly, our simulations omit global effects, and we discuss below how mechanisms such as global instabilities or radial advection of flux may be needed to sustain low β . Similarly, H+24 in particular incorporates a much wider set of physical processes — e.g., multiphase thermodynamics, accretion from a dynamic interstellar medium (which induces warps), radiation, and self gravity — which may also have relevance.

Motivated by the limitations of the shearing box in capturing some potentially important physics, in a companion paper (Guo et al., in prep) we use ATHENA simulations to study a simple model of the formation and evolution of a global disk initially dominated by a toroidal magnetic field, which forms from the inflow of a rotating gas cloud seeded with azimuthal magnetic flux. The global results in Guo et al. (in prep) are similar in many respects to the low- β state presented here and seem to exhibit a similar resolution dependence, showing a $\beta \ll 1$ midplane only when the thermal scale-height of the disk

is not resolved (see App. B). This comparison of idealized local and global results supports the idea that the low- β state is robust but that a midplane with $\beta \ll 1$ is not a generic outcome.

The idealized global simulations in Guo et al. (in prep) and the local simulations presented here still differ dramatically in physics complexity from the simulations of H+24.¹¹ It thus remains an open possibility that in some circumstances global simulations can realize a (resolved) $\beta \ll 1$ low- β state, even though the local simulations and simplified global models do not. To speculate on the conditions under which $\beta \ll 1$ may be sustained, we refer back to Fig. 13, which shows: (i) even as the system is losing net flux, it is regenerated near the midplane (just lost more slowly than it is produced) and (ii) that field is regenerated well above the midplane and sustains $\beta_{\text{mid}} \ll 1$, so long as the midplane density collapse is halted (in this case, by the grid resolution). These observations hint that the *cause* of the loss of flux (leading to $\beta_{\text{mid}} \sim 1$) could be the density collapse: in the absence of some particular scale height H_ρ for the system to “choose,” it collapses to (nearly) H_{th} . If so, then one might expect that any other physical process that halts the density collapse with $H_\rho \gg H_{\text{th}}$ might also — as a side effect — halt the loss of flux. Another (non-exclusive) possibility is the opposite: that halting the loss of flux could stop the collapse of the density.

As relates to the former possibility, there are a number of ways in which the density collapse could be halted in the global case. Other than radiation, which can provide another non-thermal pressure that supports the midplane against collapse (e.g., Jiang & Blaes 2020), the most obvious possibility is supersonic turbulence in the midplane (it must be supersonic so that the turbulent pressure P_{turb} exceeds P_{th} , thus leading to a larger scale-height and lower midplane density). As discussed extensively in H+24 and §4.1, there exist other global instabilities that can have faster growth rates than the standard MRI at $\beta \ll 1$ (Pessah & Psaltis 2005; Das et al. 2018). These are driven by global currents and thus depend on the radial gradient of the (super-thermal) toroidal field, reducing to the local MRI when $d \ln B_\phi / d \ln R = -1$ such that $\mathbf{J} \propto \nabla \times (\overline{B_\phi \hat{\phi}}) \approx r^{-1} \partial_r (r \overline{B_\phi}) \hat{z} \approx 0$ (see §4.1 and Begelman & Armitage 2023). Such instabilities could plausibly produce supersonic turbulence in global simulations, and it is possible that they would be present in H+24 but not in Guo et al.’s more idealized global simulations, given the different conditions in each. In support of this idea, we note that the B_ϕ gradient in H+24’s simulation is close to, but not exactly, $\hat{B} = -1$ (see their figure 3), as would be expected if the instability was driving the system close to marginality (see also their figure 16). If correct, this implies the existence of yet another switch-like transition between accretion states, with the system choosing between (i) ultra-low β , with active global instabilities and the Parker dynamo maintaining $\beta \ll 1$, (ii) low β , as studied here in the shearing box, with $\beta_{\text{mid}} \sim 1$, and (iii) high- β cycles. The choice between these would be determined primarily by

¹¹ This is less true for Gaburov et al. 2012 who studied a more idealized problem; indeed the idealized global model of Guo et al. (in prep) was chosen to be similar to Gaburov et al. (2012)’s calculation.

the total azimuthal and/or radial magnetic flux available, as well as $d \ln B_\phi / dR$.

In addition to the above scenario, the maintenance of $\beta \ll 1$ in a global context could be explained by various other effects, from radiation pressure and multi-phase gas structure to an additional source of magnetic flux. The latter could stop the density's collapse by maintaining $\beta \ll 1$ (i.e., the reverse causation to that discussed above) if it were sufficient to overwhelm vertical field losses. Such a source could arise as a simple consequence of radial flux advection, as discussed extensively in H+24, adding additional growth and loss terms into the $\partial_t \bar{B}_y$ equation (10), which depend on the profile and relative compression of B_ϕ and B_R as they are transported in the disk. Indeed, because of the large accretion rates, the accretion timescales in the H+24 simulation can be extremely short, of order several orbital times, and thus potentially shorter than the timescale over which the flux is lost vertically in our local simulations. While such radial advection seems insufficient to maintain $\beta \ll 1$ at the midplane in Guo et al. (in prep), these simulations explored just one class of idealized setup; other global solutions may advect flux inwards more efficiently.

Overall, clearly more work on this subject is needed. While global setups will undeniably be the most relevant for study of these issues, aspects of the Pessah & Psaltis (2005) instabilities may be possible to capture in local domains. The importance of thermodynamics, more complex initial conditions, and other physics present in var-

ious global studies should also be explored to see if they influence the magnetization in the low- β state. Whatever the outcome, there clearly exists a rich array of behaviors in strongly magnetized disks, in particular various magnetic “switches” — state transitions that depend on the magnetic-field strength and geometry. This has interesting applications for our understanding of quasars, X-ray binaries, CVs, and other high-energy accreting systems.

ACKNOWLEDGMENTS

We thank Omer Blaes, Charles Gammie, Minghao Guo, Matt Kunz, Eve Ostriker, Jim Stone, Yashvardhan Tomar, and especially Yuri Levin for useful conversations, as well as the anonymous referee who provided useful suggestions for improving the manuscript. JS acknowledges the support of the Royal Society Te Apārangi, through Marsden-Fund grant MFP-UOO2221 and Rutherford Discovery Fellowship RDF-U001804. This work was also supported in part by Simons Investigator grants from the Simons Foundation (PH, EQ) and by NSF AST grant 2107872. This research was part of the Frontera computing project at the Texas Advanced Computing Center, which is made possible by National Science Foundation award OAC-1818253. Further computational support was provided by the New Zealand eScience Infrastructure (NeSI) high performance computing facilities, funded jointly by NeSI's collaborator institutions and through the NZ MBIE. This research benefited from interactions at the Kavli Institute for Theoretical Physics, supported by NSF PHY-2309135.

REFERENCES

- Bai, X.-N., & Stone, J. M. 2013, *Astrophys. J.*, 767, 30, [10.1088/0004-637X/767/1/30](https://doi.org/10.1088/0004-637X/767/1/30)
- Balbus, S. A., & Hawley, J. F. 1991, *Astrophys. J.*, 376, 214, [10.1086/170270](https://doi.org/10.1086/170270)
- . 1998, *Rev. Mod. Phys.*, 70, 1, [10.1103/revmodphys.70.1](https://doi.org/10.1103/revmodphys.70.1)
- Begelman, M. C., & Armitage, P. J. 2014, *Astrophys. J. Lett.*, 782, L18, [10.1088/2041-8205/782/2/L18](https://doi.org/10.1088/2041-8205/782/2/L18)
- . 2023, *Mon. Not. R. Astron. Soc.*, 521, 5952, [10.1093/mnras/stad914](https://doi.org/10.1093/mnras/stad914)
- Begelman, M. C., & Pringle, J. E. 2007, *Mon. Not. R. Astron. Soc.*, 375, 1070, [10.1111/j.1365-2966.2006.11372.x](https://doi.org/10.1111/j.1365-2966.2006.11372.x)
- Brandenburg, A., Rädler, K. H., Rheinhardt, M., & Käpylä, P. J. 2008, *Astrophys. J.*, 676, 740, [10.1086/527373](https://doi.org/10.1086/527373)
- Brandenburg, A., & Subramanian, K. 2005, *Phys. Rep.*, 417, 1, [10.1016/j.physrep.2005.06.005](https://doi.org/10.1016/j.physrep.2005.06.005)
- Chandrasekhar, S. 1961, *Hydrodynamic and hydromagnetic stability*, Dover Books on Physics Series (Dover Publications)
- Coleman, M. S. B., Yerger, E., Blaes, O., Salvesen, G., & Hirose, S. 2017, *Mon. Not. R. Astron. Soc.*, 467, 2625, [10.1093/mnras/stx268](https://doi.org/10.1093/mnras/stx268)
- Das, U., Begelman, M. C., & Lesur, G. 2018, *Mon. Not. R. Astron. Soc.*, 473, 2791, [10.1093/mnras/stx2518](https://doi.org/10.1093/mnras/stx2518)
- Davis, S. W., Stone, J. M., & Pessah, M. E. 2010, *Astrophys. J.*, 713, 52, [10.1088/0004-637X/713/1/52](https://doi.org/10.1088/0004-637X/713/1/52)
- Foglizzo, T., & Tagger, M. 1994, *Astron. Astro.*, 287, 297, [10.48550/arXiv.astro-ph/9403019](https://doi.org/10.48550/arXiv.astro-ph/9403019)
- . 1995, *Astron. Astro.*, 301, 293, [10.48550/arXiv.astro-ph/9502049](https://doi.org/10.48550/arXiv.astro-ph/9502049)
- Fragile, P. C., & Sądowski, A. 2017, *Mon. Not. R. Astron. Soc.*, 467, 1838, [10.1093/mnras/stx274](https://doi.org/10.1093/mnras/stx274)
- Fromang, S. 2010, *Astron. Astro.*, 514, L5, [10.1051/0004-6361/201014284](https://doi.org/10.1051/0004-6361/201014284)
- Fromang, S., Papaloizou, J., Lesur, G., & Heinemann, T. 2007, *Astron. Astro.*, 476, 1123, [10.1051/0004-6361:20077943](https://doi.org/10.1051/0004-6361:20077943)
- Gaburov, E., Johansen, A., & Levin, Y. 2012, *Astrophys. J.*, 758, 103, [10.1088/0004-637X/758/2/103](https://doi.org/10.1088/0004-637X/758/2/103)
- Gammie, C. F., & Balbus, S. A. 1994, *Mon. Not. R. Astron. Soc.*, 270, 138, [10.1093/mnras/270.1.138](https://doi.org/10.1093/mnras/270.1.138)
- Gammie, C. F., & Menou, K. 1998, *Astrophys. J. Lett.*, 492, L75, [10.1086/311091](https://doi.org/10.1086/311091)
- Goedbloed, J. P. H., & Poedts, S. 2004, *Principles of Magnetohydrodynamics: With Applications to Laboratory and Astrophysical Plasmas* (Cambridge University Press)
- Goodman, J. 2003, *MNRAS*, 339, 937, [10.1046/j.1365-8711.2003.06241.x](https://doi.org/10.1046/j.1365-8711.2003.06241.x)
- Gressel, O. 2010, *Mon. Not. R. Astron. Soc.*, 405, 41, [10.1111/j.1365-2966.2010.16440.x](https://doi.org/10.1111/j.1365-2966.2010.16440.x)
- . 2013, *Astrophys. J.*, 770, 100, [10.1088/0004-637X/770/2/100](https://doi.org/10.1088/0004-637X/770/2/100)
- Gressel, O., & Pessah, M. E. 2015, *Astrophys. J.*, 810, 59, [10.1088/0004-637X/810/1/59](https://doi.org/10.1088/0004-637X/810/1/59)
- Guan, X., Gammie, C. F., Simon, J. B., & Johnson, B. M. 2009, *Astrophys. J.*, 694, 1010, [10.1088/0004-637X/694/2/1010](https://doi.org/10.1088/0004-637X/694/2/1010)
- Guo, M., Stone, J. M., Quataert, E., & Kim, C.-G. 2024, *Astrophys. J.*, 973, 141, [10.3847/1538-4357/ad5fe7](https://doi.org/10.3847/1538-4357/ad5fe7)
- Hameury, J. M. 2020, *Advances in Space Research*, 66, 1004, [10.1016/j.asr.2019.10.022](https://doi.org/10.1016/j.asr.2019.10.022)
- Hawley, J. F., Gammie, C. F., & Balbus, S. A. 1995, *Astrophys. J.*, 440, 742, [10.1086/175311](https://doi.org/10.1086/175311)
- Held, L. E., Mamatsashvili, G., & Pessah, M. E. 2024, *Mon. Not. R. Astron. Soc.*, 530, 2232, [10.1093/mnras/stae929](https://doi.org/10.1093/mnras/stae929)
- Hirose, S., Blaes, O., Krolik, J. H., Coleman, M. S. B., & Sano, T. 2014, *Astrophys. J.*, 787, 1, [10.1088/0004-637X/787/1/1](https://doi.org/10.1088/0004-637X/787/1/1)
- Hopkins, P. F., Grudic, M. Y., Su, K.-Y., et al. 2024a, *Open J. Astrophys.*, 7, 18, [10.21105/astro.2309.13115](https://doi.org/10.21105/astro.2309.13115)
- Hopkins, P. F., Squire, J., Su, K.-Y., et al. 2024b, *Open J. Astrophys.*, 7, 19, [10.21105/astro.2310.04506](https://doi.org/10.21105/astro.2310.04506)
- Hopkins, P. F., Squire, J., Quataert, E., et al. 2024c, *Open J. Astrophys.*, 7, 20, [10.21105/astro.2310.04507](https://doi.org/10.21105/astro.2310.04507)
- Horiuchi, T., Matsumoto, R., Hanawa, T., & Shibata, K. 1988, *Pub. Astron. Soc. Japan*, 40, 147
- Jiang, Y.-F., & Blaes, O. 2020, *Astrophys. J.*, 900, 25, [10.3847/1538-4357/aba4b7](https://doi.org/10.3847/1538-4357/aba4b7)
- Johansen, A., & Levin, Y. 2008, *Astron. Astro.*, 490, 501, [10.1051/0004-6361:200810385](https://doi.org/10.1051/0004-6361:200810385)
- Johnson, B. M. 2007, *Astrophys. J.*, 660, 1375, [10.1086/513867](https://doi.org/10.1086/513867)

- Käpylä, M. J., Vizoso, J. Á., Rheinhardt, M., Brandenburg, A., & Singh, N. K. 2020, *Astrophys. J.*, 905, 179, [10.3847/1538-4357/abc1e8](#)
- King, A. R., Pringle, J. E., & Livio, M. 2007, *Mon. Not. R. Astron. Soc.*, 376, 1740, [10.1111/j.1365-2966.2007.11556.x](#)
- King, A. R., & Ritter, H. 1998, *Mon. Not. R. Astron. Soc.*, 293, L42, [10.1046/j.1365-8711.1998.01295.x](#)
- Knobloch, E. 1992, *Mon. Not. R. Astron. Soc.*, 255, 25P, [10.1093/mnras/255.1.25P](#)
- Kotko, I., & Lasota, J. P. 2012, *Astron. Astro.*, 545, A115, [10.1051/0004-6361/201219618](#)
- Kudoh, Y., Wada, K., & Norman, C. 2020, *Astrophys. J.*, 904, 9, [10.3847/1538-4357/abba39](#)
- Lesur, G., Ferreira, J., & Ogilvie, G. I. 2013, *Astron. Astro.*, 550, A61, [10.1051/0004-6361/201220395](#)
- Lesur, G., & Ogilvie, G. I. 2008a, *Mon. Not. R. Astron. Soc.*, 391, 1437, [10.1111/j.1365-2966.2008.13993.x](#)
- , 2008b, *Astron. Astro.*, 488, 451, [10.1051/0004-6361:200810152](#)
- Machida, M., Nakamura, K. E., & Matsumoto, R. 2006, *Pub. Astron. Soc. Japan*, 58, 193, [10.1093/pasj/58.1.193](#)
- Miller, K. A., & Stone, J. M. 2000, *Astrophys. J.*, 534, 398, [10.1086/308736](#)
- Mishra, B., Begelman, M. C., Armitage, P. J., & Simon, J. B. 2020, *Mon. Not. R. Astron. Soc.*, 492, 1855, [10.1093/mnras/stz3572](#)
- Mishra, B., Fragile, P. C., Anderson, J., et al. 2022, *Astrophys. J.*, 939, 31, [10.3847/1538-4357/ac938b](#)
- Mondal, T., & Bhat, P. 2023, *Phys. Rev. E*, 108, 065201, [10.1103/PhysRevE.108.065201](#)
- Oda, H., Machida, M., Nakamura, K. E., & Matsumoto, R. 2009, *Astrophys. J.*, 697, 16, [10.1088/0004-637X/697/1/16](#)
- Pariev, V. I., Blackman, E. G., & Boldyrev, S. A. 2003, *Astron. Astro.*, 407, 403, [10.1051/0004-6361:20030868](#)
- Parker, E. N. 1958, *Astrophys. J.*, 128, 664, [10.1086/146579](#)
- Pessah, M. E., & Psaltis, D. 2005, *Astrophys. J.*, 628, 879, [10.1086/430940](#)
- Pouquet, A., Frisch, U., & Leorat, J. 1976, *J. Fluid Mech.*, 77, 321, [10.1017/S0022112076002140](#)
- Rädler, K.-H., & Stepanov, R. 2006, *Phys. Rev. E*, 73, 056311, [10.1103/PhysRevE.73.056311](#)
- Ricci, C., & Trakhtenbrot, B. 2023, *Nature Astronomy*, 7, 1282, [10.1038/s41550-023-02108-4](#)
- Rincon, F. 2019, *J. Plasma Phys.*, 85, 205850401, [10.1017/S0022377819000539](#)
- Rogachevskii, I., & Kleeorin, N. 2008, *Astron. Nat.*, 329, 732, [10.1002/asna.200811014](#)
- Ryan, B. R., Gammie, C. F., Fromang, S., & Kestener, P. 2017, *Astrophys. J.*, 840, 6, [10.3847/1538-4357/aa6a52](#)
- Salvesen, G., Armitage, P. J., Simon, J. B., & Begelman, M. C. 2016a, *Mon. Not. R. Astron. Soc.*, 460, 3488, [10.1093/mnras/stw1231](#)
- Salvesen, G., Simon, J. B., Armitage, P. J., & Begelman, M. C. 2016b, *Mon. Not. R. Astron. Soc.*, 457, 857, [10.1093/mnras/stw029](#)
- Scepi, N., Dexter, J., Begelman, M. C., et al. 2024, *Astron. Astro.*, 692, A153, [10.1051/0004-6361/202451568](#)
- Scepi, N., Lesur, G., Dubus, G., & Flock, M. 2018, *Astron. Astro.*, 620, A49, [10.1051/0004-6361/201833921](#)
- Schrinner, M., Rädler, K. H., Schmitt, D., Rheinhardt, M., & Christensen, U. 2005, *Astronomische Nachrichten*, 326, 245, [10.1002/asna.200410384](#)
- Shakura, N. I., & Sunyaev, R. A. 1973, *Astron. Astro.*, 24, 337
- Shi, J.-M., Stone, J. M., & Huang, C. X. 2016, *Mon. Not. R. Astron. Soc.*, 456, 2273, [10.1093/mnras/stv2815](#)
- Shu, F. H. 1974, *Astron. Astro.*, 33, 55
- Simon, J. B., Bai, X.-N., Armitage, P. J., Stone, J. M., & Beckwith, K. 2013, *Astrophys. J.*, 775, 73, [10.1088/0004-637X/775/1/73](#)
- Simon, J. B., Beckwith, K., & Armitage, P. J. 2012, *Mon. Not. R. Astron. Soc.*, 422, 2685, [10.1111/j.1365-2966.2012.20835.x](#)
- Simon, J. B., Hawley, J. F., & Beckwith, K. 2011, *Astrophys. J.*, 730, 94, [10.1088/0004-637X/730/2/94](#)
- Sądowski, A. 2016, *Mon. Not. R. Astron. Soc.*, 459, 4397, [10.1093/mnras/stw913](#)
- Skipper, C. J., & McHardy, I. M. 2016, *Mon. Not. R. Astron. Soc.*, 458, 1696, [10.1093/mnras/stw436](#)
- Smak, J. 1984, *Acta Astron.*, 34, 161
- Squire, J., & Bhattacharjee, A. 2014, *Astrophys. J.*, 797, 67, [10.1088/0004-637X/797/1/67](#)
- , 2015a, *Phys. Rev. Lett.*, 114, 085002, [10.1103/PhysRevLett.114.085002](#)
- , 2015b, *Phys. Rev. Lett.*, 115, 175003, [10.1103/PhysRevLett.115.175003](#)
- , 2015c, *Astrophys. J.*, 813, 52, [10.1088/0004-637X/813/1/52](#)
- , 2016, *J. Plasma Phys.*, 82, 535820201, [10.1017/S0022377816000258](#)
- Stone, J. M., Hawley, J. F., Gammie, C. F., & Balbus, S. A. 1996, *Astrophys. J.*, 463, 656, [10.1086/177280](#)
- Stone, J. M., Tomida, K., White, C. J., & Felker, K. G. 2020, *Astrophys. J. Supp.*, 249, 4, [10.3847/1538-4365/ab929b](#)
- Suzuki, T. K., & Inutsuka, S.-i. 2009, *Astrophys. J. Lett.*, 691, L49, [10.1088/0004-637X/691/1/L49](#)
- Tetarenko, B. E., Lasota, J. P., Heinke, C. O., Dubus, G., & Sivakoff, G. R. 2018, *Nature*, 554, 69, [10.1038/nature25159](#)
- Tharakkal, D., Shukurov, A., Gent, F. A., Sarson, G. R., & Snodin, A. 2023, *Mon. Not. R. Astron. Soc.*, 525, 2972, [10.1093/mnras/stad2475](#)
- Zhou, H., & Blackman, E. G. 2021, *Mon. Not. R. Astron. Soc.*, 507, 5732, [10.1093/mnras/stab2469](#)
- Zhu, Z., & Stone, J. M. 2018, *Astrophys. J.*, 857, 34, [10.3847/1538-4357/aaafc9](#)

APPENDIX

A. DEPENDENCE ON BOX SIZE

In Fig. 16 we diagnose the dependence of our results on horizontal domain size by systematically changing L_y and L_x by factors of 2 in the various simulations listed in table 2. The initial conditions and parameters are as for $\beta R0.1$ (though with $N_z = 336$ and Power-Law boundary conditions), which reach the low- β state with the default size $L_x = L_y/2 = L_z$. Changing L_x does not appear to have an effect, although it does lead to larger relative fluctuations in the mean field (not shown), while increasing L_y leads to no noticeable differences in the low- β state itself or how it is approached. However, decreasing L_y by a factor of 2 causes the system to lose its flux and enter the high- β state (the cyclic phases are not shown but do emerge at late times), while this same

(smaller) L_y , retains its flux in the low- β state if the initial β and H_{th} are also decreased (simulation $\beta 0.05$ -short). This is consistent with the idea discussed in the main text that $\beta \approx 0.1$ initial conditions lie close to the boundary where the system can reach either the low- or high- β state.

These results suggest that long-wavelength modes in y are needed to sustain the low- β state. The clear candidates are the MRI (§4.1) and/or the Parker instability (§4.2), which both have peak growth rates at finite k_y . To assess this physics, in the inset of Fig. 16 we plot $k_{\gamma, \text{max}}$, the k_y of the fastest-growing mode, for the quasi-interchange Parker instability (blue; from Eq. (9)) and the MRI (red; $k_{\gamma, \text{max}} = \Omega/v_{Ay}$), using the x - y averaged fields of $\beta R0.1$. We see that the MRI and Parker instabilities appear well resolved at small and large z , respectively, although at $z \simeq 1$, just outside of the central density hump, it is closer to marginal (especially if $k_{y0} = 2\pi/L_y$ were increased by a factor of two, as in

Name	β_{y0}	β_{x0}	β_z	$H_{\text{th}} = \sqrt{2} \frac{c_s}{\Omega}$	$N_x \times N_y \times N_z$	$(t_{\text{av}}, t_{\text{fin}}) \frac{\Omega}{2\pi}$	BCs	Notes	Outcome	$\langle \alpha \rangle$
$\beta\text{R0.1-long}$	0.1	100	∞	0.43	336^3	(10,30)	Power-law	$L_y = 40, L_x = 10$	Low- β	0.61
$\beta\text{R0.1-short}$	0.1	100	∞	0.43	$336 \times 168 \times 336$	(25,32)	Power-law	$L_y = 10, L_x = 10$	High- β	<0.05
$\beta\text{R0.1-narrow}$	0.1	100	∞	0.43	168×336^2	(10,32)	Power-law	$L_y = 20, L_x = 5$	Low- β	0.55
$\beta\text{R0.1-short-narr}$	0.1	100	∞	0.43	$168^2 \times 336$	(30,60)	Power-law	$L_y = 10, L_x = 5$	High- β	0.01
$\beta\text{R0.05-short}$	0.05	100	∞	0.31	$336 \times 168 \times 336$	(10,34)	Power-law	$L_y = 10, L_x = 10$	Low- β	0.44
$\beta\text{0.1-224}$	0.1	∞	∞	0.43	224^3	(10,40)	Power-law		Low- β	0.37
$\beta\text{0.1-168}$	0.1	∞	∞	0.43	168^3	(10,40)	Power-law		Low- β	0.31
$\beta\text{0.1-112}$	0.1	∞	∞	0.43	112^3	(10,40)	Power-law		Mixed	0.24
$\beta\text{0.1-84}$	0.1	∞	∞	0.43	84^3	(20,40)	Power-law		Mixed (see Fig. 17)	0.18
$\beta\text{0.1-56}$	0.1	∞	∞	0.43	56^3	(20,40)	Power-law	Non-stationary	Low- β	0.48
$\beta\text{0.1-36}$	0.1	∞	∞	0.43	32^3	(20,40)	Power-law		Low- β	1.8
$\beta\text{0.1-mr-lowfr}$	0.1	∞	∞	0.43	336^3	(63.7,71.5)	Outflow	Restart of $\beta\text{0.1-mr}$	Low- β	0.50
$\beta\text{0.1-lr-lowfr}$	0.1	∞	∞	0.43	224^3	(15,40)	Power-law	$\rho_{\text{flr}} = 3 \times 10^{-5}$	Low- β	0.35
$\beta\text{0.1-lr-lowerfr}$	0.1	∞	∞	0.43	224^3	(15,26)	Power-law	$\rho_{\text{flr}} = 10^{-5}$	Low- β	0.37
$\beta\text{R0.1-noshear}$	0.1	100	∞	0.43	336^3	(10,48)	Power-law	no shear	High- β	-0.014
$\beta\text{R0.1-norot}$	0.1	100	∞	0.43	336^3	(10,48)	Power-law	no rotation	High- β	0.014
$\beta\text{0.01-noshear}$	0.01	∞	∞	0.14	336^3	(20,34)	Outflow	no shear	High- β	0.17
$\beta\text{0.01-norot}$	0.01	∞	∞	0.14	336^3	(20,42)	Outflow	no rotation	High- β	0.14
$\beta\text{R0.1-NVF2-norot}$	0.1	100	100	0.43	336^3	(5,27)	Power-law	no rotation	High- β	0.17

TABLE 2

A LIST OF THE SIMULATIONS DISCUSSED THROUGH THE APPENDICES. THESE ARE USED TO TEST THE DEPENDENCE ON NUMERICAL PARAMETERS, AS WELL AS THE EFFECT OF SELECTIVELY REMOVING ROTATION OR SHEAR. NAMING CONVENTIONS AND COLUMNS ARE THE SAME AS TABLE 1.

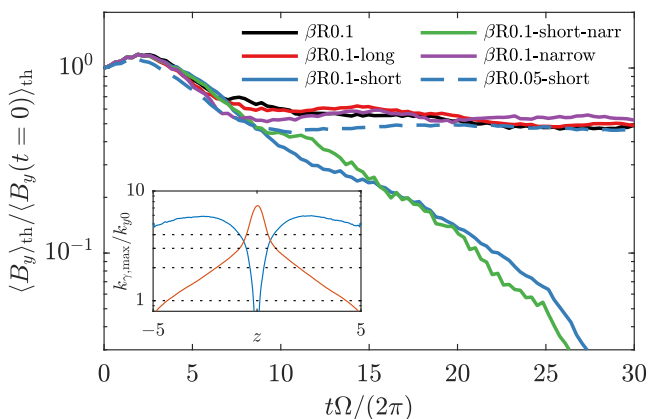


FIG. 16.— Testing the effect of changing the horizontal box dimensions on the transition to the low- β state, as diagnosed by the time evolution of $B_{y,\text{mid}}/B_{y0}$ in the main panel (see Fig. 5; plots of β_{mid} or α show similar features). The system appears robust to the choice of L_x , as indicated by $\beta\text{R0.1-narrow}$ reaching the low- β state, as well as to longer box lengths in the azimuthal direction ($\beta\text{R0.1-long}$). But, decreasing L_y by a factor of 2 in $\beta\text{R0.1-short}$ and $\beta\text{R0.1-short-narr}$ (both with $L_y = L_z$) causes an otherwise identical system to lose its flux and transition to the high- β state. At lower β and smaller H_{th} it can maintain the low- β state even at $L_y = L_z$ ($\beta\text{R0.05-short}$). The inset shows the azimuthal wavenumber $k_{\gamma,\text{max}}$ of the fastest growing Parker mode (blue; Eq. (9)) and MRI mode (red; $k_y \approx \Omega/v_{Ay}$) as a function of z for the profile of the $\beta\text{R0.1}$ run, normalized by $k_{y0} = 2\pi/L_y$. The dotted lines show the first four wavenumbers that fit in the box.

$\beta\text{R0.1-short}$). It is also worth noting that the Parker-instability analysis in §4.2 neglects shear and rotation, and these effects — especially the shear-induced time-dependence of the radial wavenumber — could change the system significantly (Foglizzo & Tagger 1994, 1995).

Given our hypothesis that MRI is necessary for maintaining turbulence in the midplane, while the Parker instability drives stronger turbulence and regenerates the field above, our tentative conclusion is that scales several times larger than that of the fastest-growing Parker quasi-interchange mode are needed to sustain the low- β state. This is qualitatively consistent with the arc-

merging picture seen in 2D Parker-instability simulations in Johansen & Levin (2008) as well as the fact that the Parker scale (9) depends on H_{th} while that of the MRI does not (thus, the MRI alone would not explain the results of $\beta\text{0.05-short}$). However, we cannot rule out other possible explanations at the present time and a more detailed study is needed.

B. DEPENDENCE ON RESOLUTION

We explore the dependence of the results on numerical resolution via a set of simulations with successively fewer grid points and the same parameters as $\beta\text{0.1-mr}$ (see table 2). This reveals interesting non-monotonic behavior, illustrated in the top panel of Fig. 17; the transport level decreases with coarsening resolution up to some point (around $N_z = 56$ here), then suddenly increases again to $\alpha \gtrsim 1$. This behavior can be explained by appealing to the phenomenology of the $\beta \ll 1$ state described in §5.5. If the resolution is sufficiently fine that the thermal density profile can be resolved, α decreases with coarsening resolution because the midplane turbulence amplitude decreases¹² (not shown; the turbulence amplitude in the corona is not a strong function of resolution). As the turbulence level drops, the density in the midplane collapses to the thermal profile across a wider range in z , and thus starts to resemble the high- β state, reaching $\beta > 1$ in the midplane in poorly resolved cases. This is illustrated in the lower panel of Fig. 17 for $\beta\text{0.1-84}$ (cf. Fig. 4). However, at resolutions below $\simeq 1.5$ zones per H_{th} for this setup ($\beta\text{0.1-56}$ has 1.7 zones per H_{th}), the density collapse is halted by the grid itself, maintaining a $\beta \ll 1$ midplane as a side effect. The midplane turbulence also maintains a larger amplitude, perhaps via overshoot from the Parker-unstable atmosphere, thus causing much larger transport (the $\beta\text{0.1-32}$ simulation also has stronger outflows and has lost around half its density by $t\Omega/2\pi = 40$).

This behavior is broadly consistent with that discussed

¹² Note that this is the reverse of the behavior seen at high resolution in the high- β state, where the turbulence amplitude drops with finer resolution (Ryan et al. 2017). Presumably this difference arises because the low- β state involves larger-scale fluctuations and has a stronger mean field (see Fig. 3).

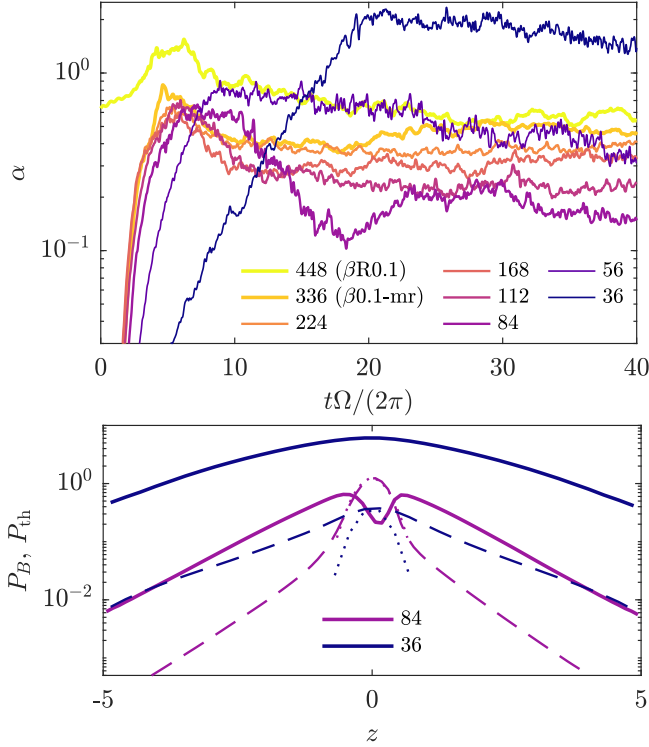


FIG. 17.— Dependence of the low- β state on numerical resolution. The top panel shows $\alpha(t)$ for a set of nearly identical simulations with $H_{\text{th}} = 0.43$ ($\beta_{y0} = 0.1$) but with different N_z as labeled in the legend (all cases have $N_x = N_y = N_z$). The bottom panel shows the time-averaged mean magnetic and thermal pressure profiles (solid and dashed lines, respectively), for the case with minimum transport ($N_z = 84$) and the coarsest-resolution case, with high transport ($N_z = 32$; we normalize such that $\int dz P_{\text{th}} = 1$). Finer resolution cases approach those shown in the main text (Figs. 4 and 8). We see interesting non-monotonic behavior: if the thermal midplane is resolvable (for $N_z \gtrsim 56$ here), the level of turbulence, and thus α , decreases with coarsening resolution, which also enhances the collapse to the thermal profile in the midplane; if the midplane is not resolvable ($N_z \lesssim 56$) the flux is maintained, giving a $\beta \ll 1$ midplane with significantly larger transport.

in the main text, although there do also appear to be important effects related to L_z/H_{th} and/or the initial conditions. In simulation $\beta 0.001$, which has $\simeq 1.1$ zones per H_{th} like $\beta 0.1-32$, but with a much smaller H_{th}/L_z , the density collapse is also supported by the resolution and it maintains a high-transport $\beta \ll 1$ midplane. However, $\beta 0.01$ and $\beta 0.01\text{-hr}$, which have resolutions per H_{th} similar to $\beta 0.1-112$ and $\beta 0.1-224$ respectively, maintain $\beta < 1$ in the midplane, albeit with a nearly thermal density profile across a wider range of z/H_{th} and a flatter P_B profile (see Figs. 4 and 10c). Similarly $\beta 0.1\text{-tall}$ has a transport level somewhat less than half that of $\beta 0.1-224$, which has the same resolution per H_{th} but a smaller vertical extent (the different boundary conditions may also be important in this difference, since we see from table 1 that Outflow conditions lead to somewhat lower $\langle \alpha \rangle$). While some of these aspects remain incompletely understood and worthy of further study, a full investigation is beyond the scope of this work.

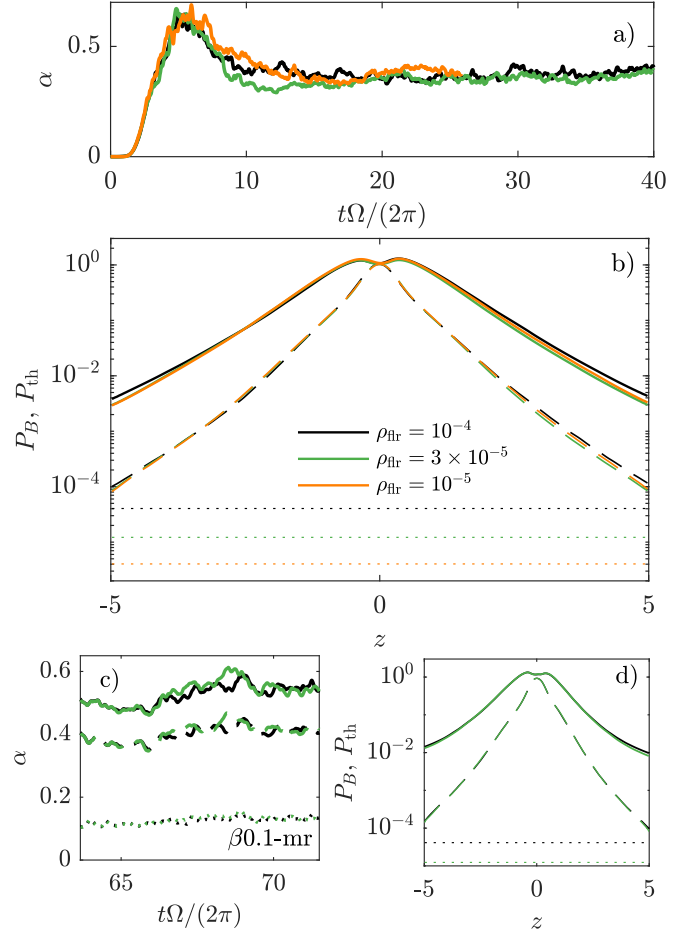


FIG. 18.— Panels a-b show the effect of changing the density floor below the default value of $\rho_{\text{flr}} = 10^{-4}$ by a factor of $\simeq 3$ ($\beta 0.1\text{-lr-lowflr}$; $\rho_{\text{flr}} = 3 \times 10^{-5}$) and 10 ($\beta 0.1\text{-lr-lowerflr}$; $\rho_{\text{flr}} = 10^{-5}$). Panel (a) shows $\alpha(t)$, while (b) shows the time-averaged density and pressure profiles, as in Fig. 17. The horizontal dotted lines illustrate the density floor in each case. Panels (c)-(d) show the similar test of restarting $\beta 0.1\text{-mr}$ at $t\Omega = 400$ with a lower floor $\rho_{\text{flr}} = 3 \times 10^{-5}$.

C. THE EFFECT OF THE DENSITY FLOOR

Most simulations in the main text impose a floor on the density at $\rho_{\text{flr}} = 10^{-4}$ of the initial central density, which is important for stabilizing the numerical scheme and allowing somewhat larger timesteps. While undesirable, this is needed because the large v_A and highly supersonic turbulence at large z cause frequent code crashes unless a very conservative CFL number is used ($\lesssim 0.1$), significantly increasing the cost of the simulations (which are already far more expensive than those in the high- β regime). While the low- β simulations studied in the main text do not show any obvious effects and mostly have a minimum mean density that remains a factor of $\simeq 2-3$ above the chosen floor, it is important to check that the maintenance of the low- β state does not depend on ρ_{flr} .

We do this through two sets of simulations that change ρ_{flr} in otherwise identical setups. In the first set ($\beta 0.1-224$, $\beta 0.1\text{-lr-lowflr}$ and $\beta 0.1\text{-lr-lowerflr}$), we decrease ρ_{flr} by factors of $\simeq 3$ and 10, starting from the standard Gaussian initial conditions. The time evolution of the transport and time-averaged profiles are shown in Fig. 18a-b, demonstrating no statistically significant differences in

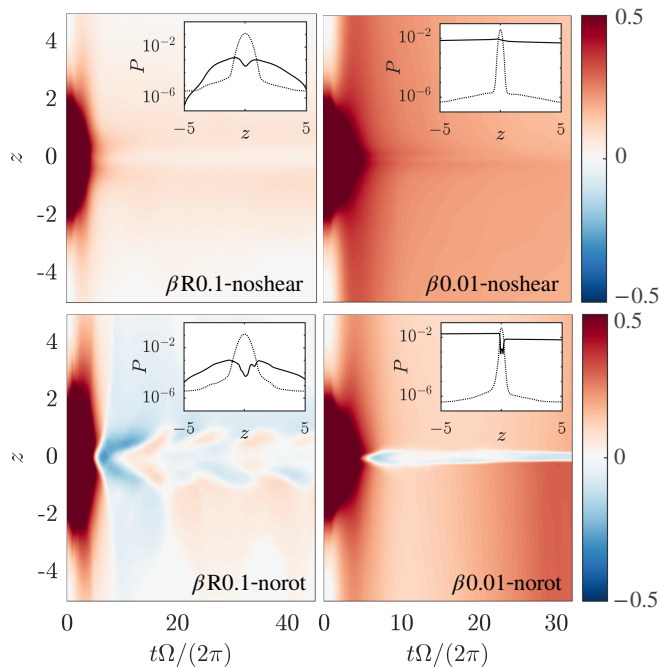


FIG. 19.— Testing the physical ingredients needed to sustain the low- β state, illustrating space-time ‘butterfly’ plots for various simulations. The top two panels remove the mean shear flow but keep Coriolis effects by setting $q = 0$ ($\beta R0.1$ -noshear and $\beta 0.01$ -noshear); the bottom panels remove the effect of rotation but retain the mean shear and the vertical gravity ($\beta R0.1$ -norot and $\beta 0.01$ -norot). In each case, the inset shows the $P_B = \overline{B_y^2}/8\pi$ (solid) and $P_{\text{th}} = c_s^2 \bar{\rho}$ (dotted) time-averaged over the steady state. All fail to maintain midplane magnetic flux.

the steady state, other than a slightly (factor $\simeq 1.1$ - 1.2) lower density towards the domain’s edge, which also decreases $\overline{B_y}$ due to force balance. The initial evolution is somewhat different because the density floor impacts the initial Gaussian density profile near the edge of the domain; this in itself is not cause for concern, since we are interested in the initial evolution only insofar as it determines the transition into the low- or high- β quasi-steady states.

The other test is to restart a simulation in a well-formed low- β state ($\beta 0.1$ -mr at $t\Omega = 400$) with $\rho_{\text{fir}} = 3 \times 10^{-5}$, the results of which are shown in Fig. 18c-d. Although the detailed evolution starts to diverge at later times, a consequence of the system being chaotic, differences in the time averaged quantities are small even in the lowest-density regions at the edge.

We note that these lower-floor simulations are at least $\simeq 3$ - 4 times more expensive computationally than those with $\rho_{\text{fir}} = 10^{-4}$, making them impractical for production simulations. Other methods should be explored in future work, particularly mesh refinement in the midplane or Lagrangian numerical schemes, which will alleviate these issues as a result of their larger grid spacing in low- ρ regions.

D. THE NECESSITY OF SHEAR AND ROTATION

To help diagnose the mechanism(s) by which the low- β state is maintained, in Fig. 19 we rerun two cases that transition into the low- β state in the standard shearing box ($\beta R0.1$ and $\beta 0.01$), but selectively remove either shear or rotation. The purpose of these modifications is

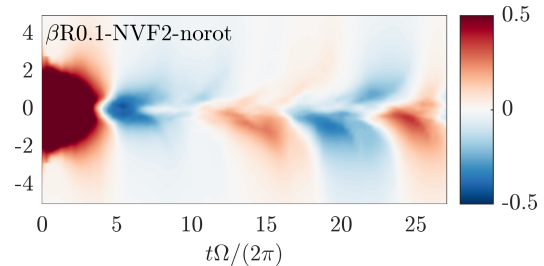


FIG. 20.— Space-time butterfly plot showing $\overline{B_y}$ for simulation $\beta R0.1$ -NVF2-norot, which has a $\beta_z = 100$ vertical flux, but with rotational effects removed. The system does not sustain the strong $\beta \lesssim 1$ azimuthal field that occurs with rotation (cf. Fig. 9).

not to explore physically relevant scenarios, but rather as numerical experiments to probe the important physics. Removing the shear simply involves setting $q = 0$ in Eqs. (1a) to (1c), while removing rotation is achieved by dropping the first two terms on the second line of Eq. (1b), or equivalently, by taking the limit $\Omega \rightarrow 0$ with $q\Omega = S = \text{const.}$ Both cases retain the vertical stratification via $-\rho\Omega^2 z \hat{z}$.

The top two panels of Fig. 19 show the effect of removing the mean shear flow; these clearly do not maintain interesting dynamics. The flux continuously escapes in $\beta R0.1$ -noshear, while P_B becomes flat in $\beta 0.01$ due to its Outflow boundary conditions, and both develop perfect thermal profiles in the midplane. The detailed structure at larger z is affected by the density floor and so is untrustworthy, but the obvious difference with Fig. 2 nonetheless clearly demonstrates the importance of the shear.

As discussed in §4.1, removing rotation kills the MRI, as well as changing the turbulence properties and Parker instability. The lower panels of Fig. 19 show $\beta R0.1$ -norot and $\beta 0.01$ -norot in which the rotation is artificially removed. Neither of these maintain the low- β state, developing a thermally dominated midplane. Interestingly, dynamo cycles develop in $\beta R0.1$ -norot, despite the lack of the MRI. Assuming these are of similar origin to those in the high- β state (given they have a similar period and structure) it is clear that the nomenclature ‘MRI dynamo cycles’ is not accurate. Given this system’s small H_{th} and the density floor, this would be worth a dedicated study in future work. In the lower- β case ($\beta 0.01$ -norot) we do not see this feature, presumably due to the poorly resolved midplane and outflow boundary conditions that lead to $P_B \approx \text{const.}$ at $z \gtrsim 2H_{\text{th}}$. Notwithstanding, given the clear difference with $\beta 0.01$, we can conclude that rotation is crucial for maintaining the low- β state.

In Fig. 20, we remove the rotation for a case with a strong vertical field $\beta_z = 100$. This causes the system to lose its azimuthal flux, generating cyclic behavior in $\overline{B_y}$ and a thermal midplane. This is similar to the high- β ZNVF system (cf. Fig. 19) although with somewhat stronger mean-field cycles. The behavior is consistent with our interpretation in §5.4 that the NVF low- β state is effectively a single large-scale MRI mode, which requires rotation to sustain itself. It also supports the idea that the dynamo cycles are not a consequence of the MRI, which does not exist in the absence of rotation.

This paper was built using the Open Journal of Astrophysics L^AT_EX template. The OJA is a journal which

provides fast and easy peer review for new papers in the **astro-ph** section of the arXiv, making the reviewing process simpler for authors and referees alike. Learn more at <http://astro.theoj.org>.